JGR Atmospheres

RESEARCH ARTICLE
10.1029/2021JD034683

Special Section:
SOUTHTRAC-GW: An airborne field campaign to explore gravity wave dynamics at the world's strongest hotspot

Key Points:

- Middle atmospheric lidar temperature measurements were performed at the Southern Andes gravity wave hot spot with unprecedented cadence
- Exceptional wave events were observed in winter, resulting in temperature deviations from the monthly mean of 25–55 K
- Gravity wave (GW) potential energies show conservative growth rates in the stratosphere and a saturation limit in the mesosphere during winter

Correspondence to:
R. Reichert,
robert.reichert@dlr.de

Citation:
Reichert, R., Kaifler, B., Kaifler, N., Dörnbrack, A., Rapp, M., & Hormaechea, J. L. (2021). High-cadence lidar observations of middle atmospheric temperature and gravity waves at the Southern Andes hot spot. *Journal of Geophysical Research: Atmospheres*, *126*, e2021JD034683. https://doi.org/10.1029/2021JD034683

Received 29 JAN 2021
Accepted 18 OCT 2021

Author Contributions:
Conceptualization: R. Reichert, B. Kaifler, A. Dörnbrack, M. Rapp
Data curation: R. Reichert, B. Kaifler, A. Dörnbrack
Formal analysis: R. Reichert
Funding acquisition: B. Kaifler, N. Kaifler, M. Rapp
Investigation: B. Kaifler, N. Kaifler
Methodology: R. Reichert

High-Cadence Lidar Observations of Middle Atmospheric Temperature and Gravity Waves at the Southern Andes Hot Spot

R. Reichert[1], **B. Kaifler**[1], **N. Kaifler**[1], **A. Dörnbrack**[1], **M. Rapp**[1,2], **and J. L. Hormaechea**[3]

[1]Deutsches Zentrum für Luft- und Raumfahrt, Institut für Physik der Atmosphäre, Wessling, Germany,
[2]Meteorologisches Institut, Ludwig-Maximilians-Universität, Munich, Germany, [3]Estación Astrónomica Río Grande, Facultad de Ciencias Astronómicas y Geofísicas, Universidad Nacional de La Plata and CONICET, Rio Grande, Argentina

Abstract The Southern Andes are the strongest hot spot for atmospheric gravity waves (GWs) in the stratosphere. Yet, until recently, no high-cadence measurements of GWs within the middle atmosphere were available in this region. Therefore, the COmpact Rayleigh Autonomous Lidar (CORAL) was deployed to the Estación Astrónomica Río Grande (53.7°S, 67.7°W), Argentina, to obtain temperature profiles up to 100 km altitude. CORAL operates autonomously and obtained measurements during roughly two thirds of all nights between November 2017 and October 2020. The excellent measurement coverage allows for the quantification of GW properties at the hot spot with great detail. The hot spot nature of this region is reflected in nightly mean temperature profiles showing deviations from the monthly mean in the order of 25–55 K in each winter month. This is connected to winter mean growth rates of GW potential energy (E_p), which are to our knowledge the largest ever reported in the stratosphere. The monthly mean E_p profiles show a mesospheric limit of ∼100 $\mathrm{J kg^{-1}}$, indicating a saturated GW spectrum at altitudes above 60 km. The winter mean power spectral density also reaches the saturation limit here. Moreover, we investigated the distribution of vertical wavelengths using our novel diagnostic technique WAVELET-SCAN. It reveals waves with vertical wavelengths that are mostly between 10 and 16 km but also can exceed 25 km in rare occasions.

1. Introduction

The observation of atmospheric gravity waves in the middle atmosphere is a challenging task and calls for highly sophisticated instrumentation. However, the effort is worthwhile as the propagation of gravity waves (GWs) is a key mechanism in coupling all layers of the atmosphere, transferring energy and momentum from their source regions to the locations where they dissipate (e.g., Fritts & Alexander, 2003). To observe properties of GWs at a specific location, a suitable tool is a lidar system because it samples a large altitude range from the lower stratosphere to the lower thermosphere with high temporal and vertical resolutions. This work presents the first high-cadence middle atmospheric lidar temperature data set from a location in the lee of the Southern Andes at the east coast of Argentina for the period November 2017 to October 2020.

GWs in the middle atmosphere over the Southern Andes have been the focus of multiple studies (e.g., Eckermann & Preusse, 1999; Hindley et al., 2015, 2020; Hoffmann et al., 2013; Preusse et al., 2002; Wright et al., 2016, 2017). At this hot spot for middle atmospheric GWs, the majority of observed modes are mountain waves (MWs), which are excited by strong air flow across the Andean topography. During austral winter, favorable propagation conditions due to the prevailing stratospheric westerlies lead to exceptional large GW momentum flux, which is on average 10 times larger than anywhere else on the globe (Hindley et al., 2020). The direction of the momentum flux above the Southern Andes is found to be southwestward (Wright et al., 2017), which indicates that MWs propagate meridionally toward the core of the stratospheric polar night jet (PNJ). These observations are confirmed by raytracing simulations and numerical modeling (Jiang et al., 2013; Preusse et al., 2002; Sato et al., 2009). A comprehensive overview over GW properties in the Southern Andes region is given by Wright et al. (2016) who found evidence for wave dissipation in the mid-stratosphere in summer and conservative, non-dissipative vertical propagation in winter.

Project Administration: B. Kaifler, M. Rapp, J. L. Hormaechea
Resources: J. L. Hormaechea
Software: R. Reichert, B. Kaifler, N. Kaifler
Supervision: M. Rapp
Visualization: R. Reichert
Writing – original draft: R. Reichert
Writing – review & editing: R. Reichert, B. Kaifler, N. Kaifler, A. Dörnbrack, M. Rapp

The aforementioned observations are predominantly based on satellite data. Depending on the viewing geometry, the resolution is high in the vertical, but coarse in the horizontal direction (limb soundings) or vice versa (nadir soundings) (Alexander & Barnet, 2007; Alexander et al., 2008; Eckermann & Preusse, 1999; Ern et al., 2004). Due to the observation through various atmospheric layers, GW signatures are smoothed and observed amplitudes are damped. Besides, polar-orbiting satellites mostly perform measurements only twice a day above the same location and thus lack information on the temporal evolution of wave events. High-resolution long-term lidar measurements, such as those presented in this study, can capture both seasonal evolution and diurnal variability of GWs in the middle atmosphere that is not available from satellite measurements. In addition, the ground-based lidar measurements provide an ideal data set for comparison with the results of high-resolution numerical modeling (e.g., Kaifler et al., 2020).

The CORAL instrument was deployed to the Estación Astronómica Río Grande (EARG) on Tierra del Fuego in late November 2017. CORAL is a ground-based Rayleigh lidar, which conducted measurements in previous campaigns and has proven its reliability in terms of automatic operation and minimal maintenance (Ehard et al., 2017; Kaifler et al., 2017, 2018; Reichert et al., 2019; N. Kaifler et al., 2020). Recently, CORAL was deployed to prepare airborne Rayleigh lidar observations of MWs over the Southern Andes during the SOUTHTRAC-GW (Southern Hemisphere Transport, Dynamics, and Chemistry-Gravity Waves) campaign and to document the stratospheric temperature evolution in 2019 (see Figure 6 in Rapp et al., 2021). It was specifically designed for fully automatic observations of middle atmospheric temperature between 15 and 100 km altitude. Since no operators are needed to run the instrument, it probes the atmosphere whenever the night sky is clear (Kaifler & Kaifler, 2021). For the first time, the high cadence of observations allows for investigation of variations in temperature and GW activity in the middle atmosphere on a broad range of time scales, ranging from seasonal over day-to-day to hourly variations. Recently, Kaifler et al. (2020) investigated a long-lasting large-amplitude MW event that CORAL observed in June 2018. They calculated momentum fluxes and GW drag, compared them to high-resolution ECMWF data and found that the stratospheric circulation was significantly affected even far downwind. They conclude that 8% of the GW events occurring during winter are responsible for 30% of the total GW potential energy.

The GW potential energy can be derived from the lidar temperature measurements. Their values depend primarily on the ratio between the temperature disturbances and the background. Multiple approaches exist in order to separate the atmospheric background from GW signatures (Ehard et al., 2015; Gardner & Taylor, 1998; Whiteway & Carswell, 1995; Yamashita et al., 2009). In this study, we first subtract a climatological background, which comprises seasonal oscillations and apply a fifth-order Butterworth high-pass filter in the vertical direction afterward. The temporal as well as vertical evolution of GW potential energy contains information about the GW activity in general and regions of conservative propagation and of wave dissipation can be determined. Baumgaertner and McDonald (2007) report of log-normally distributed wave energies in the stratosphere with only a few events carrying large portions of the total energy. Here, our CORAL measurements are ideally suited to document the seasonal development of the energy spectra. Furthermore, due to high temporal resolution of the CORAL data, the intermittency can be quantified.

If a few GW events are responsible for the majority of the total GW energy, its frequency distribution becomes uneven. In this context, the community speaks of GW intermittency, which describes the irregular occurrence of large-energy bursts that interrupt the dynamics of a periodic system (Strogatz, 1996). One measure to estimate GW intermittency is the Gini coefficient (Alexander et al., 2016; Minamihara et al., 2020; Plougonven et al., 2013; Wright et al., 2013). GW intermittency is an important parameter because it indicates the extent to which the GW momentum flux deviates from a continuous mean flux. Based on SABER measurements Wright et al. (2013) have shown that the Gini coefficient barely changes between 25 and 65 km above the southern tip of South America.

From Wright et al. (2013) and Preusse et al. (2002) we know that MWs with vertical wavelengths up to 25 km exist. However, most lidar studies apply high-pass filter with 20 km or even 15 km cutoff due to the possible leakage of energy from tides and planetary waves into derived GW potential energies (Alexander et al., 2011; Chu et al., 2018; Kaifler, Lübken, et al., 2015; Mzé et al., 2014). To obtain a realistic picture of the distribution of vertical wavelengths we developed a new diagnostic tool called WAVELET-SCAN, which combines the continuous wavelet transformation (CWT) (Torrence & Compo, 1998) with a clustering algorithm. While the CWT has been used before to study dominant vertical wavelengths in lidar data (Baumgarten et al., 2017; Kaifler, Kaifler, et al., 2015; Reichert et al., 2019), the addition of the clustering algorithm allows the identification, separation, and discrete analysis of superimposed wave packets. Thus, with WAVELET-SCAN the properties of wave packets with weaker amplitudes can be adequately represented in the distributions.

Table 1
Runtime Hours and Number of Nights With Measurements for Each Month and Year Between November 24, 2017 and October 20, 2020

Month/Year	2017	2018	2019	2020	Total
Jan		18.0	36.8	43.8	98.6
		9	21	19	49
Feb		57.5	53.5	70.8	181.8
		17	20	24	61
Mar		91.0	83.8	108.8	283.6
		28	20	23	71
Apr		117.8	92.3	144.3	354.4
		22	20	28	70
May		151.8	174.5	142.3	468.6
		25	24	23	72
Jun		188.3	112.5	160.8	461.6
		25	19	25	69
Jul		154.0	82.0	153.5	389.5
		24	14	22	60
Aug		111.3	46.3	143.8	301.4
		23	8	27	58
Sep		86.5	-	101.0	168.5
		26	-	24	45
Oct		76.0	65.0	62.5	141.0
		19	19	15	38
Nov	5.8	37.0	64.8		107.6
	4	16	24		44
Dec	16.5	35.0	33.5		85.0
	9	16	17		42
Total	22.3	1124.2	845.0	1050.1	3041.6
	13	250	206	210	679

Note. CORAL did not perform any measurements in September 2019 due to technical issues.

The primary goal of this study is to overview the CORAL data set and demonstrate the scientific merits of high-resolution lidar observations conducted at high cadence. We see the results of this work as important additions to what has already been learned about this GW hot spot through previous studies. We will address the following questions. What is the fraction of MWs, that is, waves characterized by uniform horizontal phase lines in time-height diagrams, in our lidar data? What is the seasonal variability of the GW potential energy? Do our CORAL measurements confirm conservative wave propagation in the winter stratosphere? What is the magnitude of the GW intermittency above Río Grande? What can we say about the distribution of vertical wavelengths?

The article is structured in five sections. Section 2 presents the evolution of the nightly mean temperatures of the middle atmosphere from 2017 to 2020, discusses the seasonal dependence of the monthly mean temperature profiles, and highlights extraordinary temperature soundings above Río Grande during large-amplitude MW events. The methodology to calculate GW potential energies and our novel diagnostic technique WAVELET-SCAN are introduced in Section 3. In the subsequent Section 4, we present the seasonal variation of GW potential energy, discuss the potential energy as function of altitude, conduct a spectral analysis of sub-seasonal temperature perturbations, and identify stationary as well as up- and downward propagating waves in the CORAL data. Section 5 discusses the implications of our results in the geophysical context of the Southern Andes hot spot and Section 6 draws conclusions.

2. CORAL Temperature Data Set

CORAL is a Rayleigh backscatter lidar designed for measurements of middle atmospheric temperature up to 100 km altitude (Kaifler & Kaifler, 2021). It was built by the German Aerospace Center (DLR) and installed at the EARG in Río Grande (53.7°S, 67.7°W), Argentina in late November 2017. The lidar system is mobile and designed for remote automatic operation to maximize measurement hours. To date, (October 20, 2020) CORAL obtained 3,042 hours of high-quality data during nighttime and whenever weather conditions allowed for it. The duration of a single measurement ranges from 1 h to a maximum of 15 h, the latter being only possible during long nights in winter. Runtime hours and number of measurement nights are listed for each month and year in Table 1.

The maximum number of measurement hours per month was obtained in June 2018 with a total of 188 h and an average of 7.5 h measurement per night. The time between dusk and dawn (solar elevation angle $<-9°$) is the potential run-time as CORAL lacks daylight filters and thus operates only in darkness. Measurements cover 42% of the potential run-time in June 2018. Between June 16 and June 23, 2018 a long lasting MW was nearly continuously observed (Kaifler et al., 2020). The recording of such events demonstrates the advantage of autonomous lidar measurements as GW properties can be investigated over a larger period. In 2018, a maximum of 1,124 h (31% of potential run-time) was obtained within a total of 250 measurement nights, resulting in an average of 4.5 h measurement per night. The run-time in 2019 is 24% lower compared to 2018 due to a 7-week-long downtime caused by technical issues. In 2020, we collected even

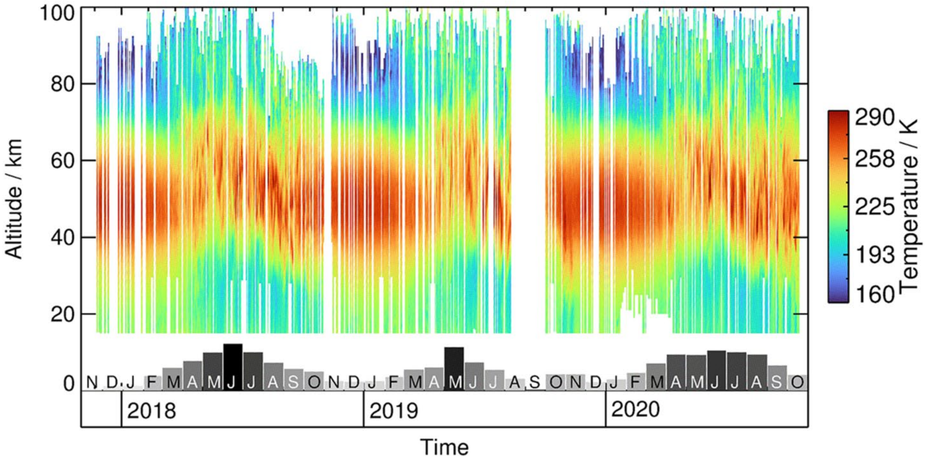

Figure 1. Nightly mean temperature profiles obtained from November 24, 2017 till October 20, 2020. Gray bars below indicate the monthly measurement duration.

more data than in 2018 with on average 5.0 h measurement per night. In addition, we obtained record-high measurement durations from January to April as well as August and September.

Temperature profiles are provided with different temporal and vertical resolutions (e.g., Reichert et al., 2019). In the following analysis temperature data are used at 900 m vertical and 60 min time resolution computed on a grid of 100 m and 15 min. The annual average mean temperature precision in the altitude ranges 15–70 km and 70–100 km is 0.3 and 4.2 K, respectively. The temperature errors include the effect of photon noise and are derived performing Monte Carlo simulations (see Kaifler & Kaifler, 2021, for details).

2.1. Nightly Mean Profiles

All nightly mean temperature profiles are displayed in Figure 1. At the bottom, monthly measurement durations are indicated with gray bars. White areas in Figure 1 mark times and altitude regions where no temperatures were retrieved. High concentrations of stratospheric aerosols caused by Australian bushfires prevented reliable temperature measurements in the lower stratosphere in austral fall 2020 (Ohneiser et al., 2020). Hence, we had to discard a large portion of temperature data between 15 km and ∼20 km in February and March 2020. Only two further data gaps occurred due to technical issues with the instrument. The first appeared when a partial failure in the laser power supply caused a decrease in laser power, resulting in a reduced achievable maximum altitude in the time frame August 18, 2018 to November 14, 2018. The second period began on August 14, 2019 when a failed heating led to freezing of coolant inside the laser and resulted in permanent damage. A replacement laser unit was shipped to Río Grande, which took about 6 weeks. This data gap covers the period of the SOUTHTRAC-GW campaign. The lidar started operating again on October 2, 2019.

The summer temperature profiles (Nov–Feb) appear smooth and undisturbed in contrast to winter profiles (Mar–Oct). We consider the temperature maximum to be the stratopause as well as the temperature minimum above 80 km to be the mesopause. In summer, the stratopause is at ∼50 km and the mesopause at ∼85 km. Sufficiently low temperatures in the summer mesopause have also led to the observation of a few noctilucent clouds, which are not the subject of this work though. The winter stratopause is cooler and elevated, and migrates downwards at the end of winter. Winter profiles show greater night-to-night variability than summer profiles.

2.2. Monthly Mean Profiles

The monthly mean temperature profiles provide a quantitative insight into the temperature structure of the middle atmosphere above Río Grande. Figure 2 shows monthly averages of nightly mean temperature

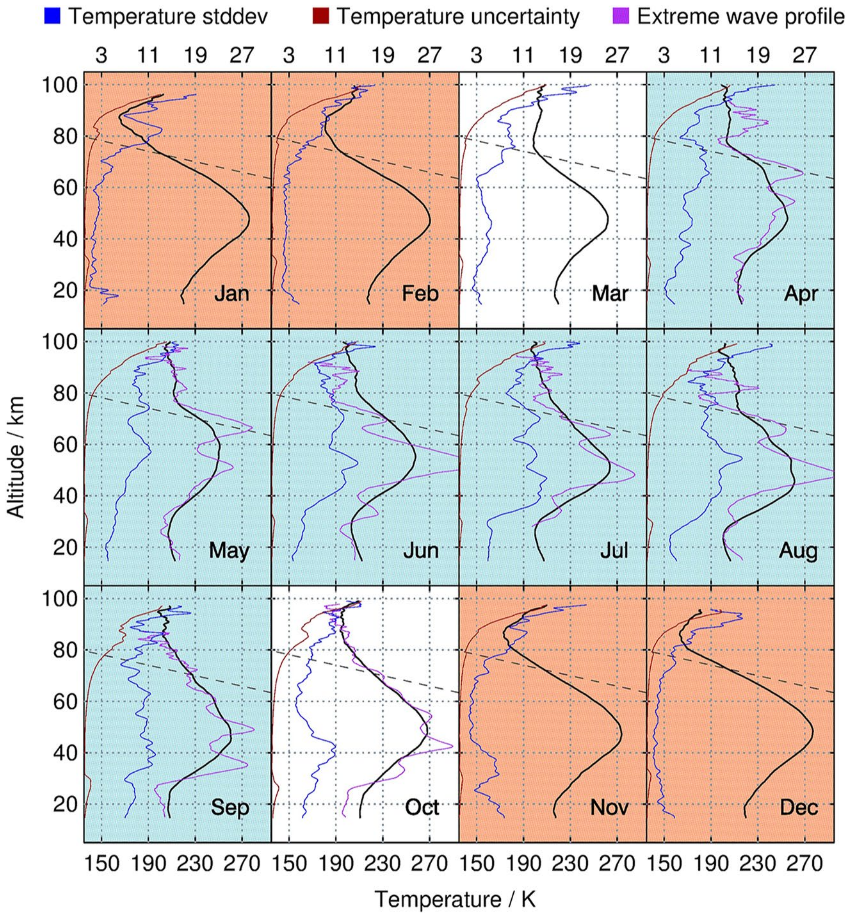

Figure 2. Monthly averages of nightly mean temperature profiles (black) and extreme wave profiles (purple) refer to the lower axis. Monthly averages of standard deviation of nightly mean temperature profiles (blue) and of nightly mean temperature uncertainty (red) refer to the upper axis. The shown profiles incorporate data from November 2017 till October 2020. The adiabatic lapse rate is sketched as black dashed line. Blue background: winter months and red background: summer months. See Table 1 for the number of measurement hours.

profiles as well as corresponding standard deviations and temperature uncertainties. In addition, in order to highlight the extraordinary wave amplitudes we show one measurement each winter month exhibiting the largest temperature deviation from the monthly mean. We call these profiles “extreme wave” profiles. Only measurements with at least 3 h duration are taken into account.

In the austral summer month of January, the stratopause is pronounced with a maximum temperature of 275 K at 48 km altitude. The mesopause is located at ∼85 km with a minimum mean temperature of 160 K. The standard deviation has a small value of 2.4 K between 15 and 70 km, which indicates a dynamically quiet stratosphere and lower mesosphere. A larger temporal variability is observed in the mesosphere, lower thermosphere region (MLT), where the standard deviation between 70 and 100 km increases to 10.3 K. Please note that temperature standard deviations are larger than temperature uncertainties at all altitudes. This illustrates that the temperature standard deviation is primarily influenced by geophysical processes and not by uncertainties in the temperature retrieval.

From February to May, the stratopause cools from 275 to 248 K and rises simultaneously from 48 to 56 km. In the same period the mesopause warms from 160 to 200 K and rises from ∼85 km to >100 km, that is, to the top or even outside of our measurement range. While the mesopause in January and February is identified by a pronounced temperature minimum, a nearly isothermal region appears between 75 and 100 km in March, April, and May. In the following months, a constant negative temperature gradient in the MLT suggests that the mesopause is located above 100 km as observed by for example, Gerding et al. (2008); Yuan et al. (2019) at mid-latitude northern hemisphere sites. Autumn temperature standard deviations increase to 6.7 K between 15 and 70 km and remain constant at 10.6 K in the MLT.

In the following winter months, large average temperature standard deviations of 10.4 K are observed in the altitude range 15–70 km. From June to August we notice a rapid increase in temperature standard deviation of ∼10 K from the lower to the upper stratosphere (∼30–40 km). The upper stratosphere is most stably stratified and largest positive temperature gradients of up to 4.8 K km^{-1} are found in August. From August onwards, the observed developments reverse in time. Temperature standard deviations below 70 km decrease and a pronounced mesopause establishes at ∼85 km in November and gradually cools, while the stratopause warms.

All extreme wave profiles in winter show a maximum deviation from the monthly mean in the order of 25–55 K. The comparison with the adiabatic lapse rate (see Figure 2) suggests that the large negative temperature gradients occurring above the stratopause are limited by convective instability. By considering the position of maxima and minima, one can estimate approximately the vertical wavelength of those extreme waves. It ranges from 10 to 20 km.

3. Methods

The high cadence of our measurements allows a robust statistical analysis. We start with the analysis of GW potential energy per mass. In extension to that, we also derive conservative growth curves. Second, we present our new diagnostic technique WAVELET-SCAN. It combines one-dimensional wavelet analysis with a clustering algorithm to infer superimposed wave features in lidar temperature data. For evaluation purposes of WAVELET-SCAN results, we introduce the two-dimensional kernel density estimation (KDE). Finally, we describe in short the two-dimensional wavelet analysis, which is used to estimate the contribution of stationary as well as apparently up- and downward propagating waves.

3.1. GW Potential Energy

GW potential energy per mass E_p is often used as proxy for the GW activity in lidar observations (e.g., Alexander et al., 2011; Baumgarten et al., 2017; Kaifler, Lübken, et al., 2015; Mzé et al., 2014; Whiteway & Carswell, 1995; Whiteway et al., 1997; Wilson et al., 1991). E_p per unit mass is commonly defined as

$$E_\mathrm{p} = \frac{1}{2}\frac{g^2}{N^2}\overline{\left(\frac{\tilde{T}}{T_\mathrm{BG}}\right)^2} \tag{1}$$

The GW potential energy is proportional to the squared GW-induced relative temperature perturbation $T_r' = \frac{\tilde{T}}{T_\mathrm{BG}}$, which is the perturbation amplitude $\tilde{T}$ divided by the background temperature T_BG. The term $g = g(z)$ is the acceleration due to Earth's gravity as function of altitude z and N is the buoyancy frequency (e.g., Wilson et al., 1991; Whiteway et al., 1997; Rauthe et al., 2008). In order to derive E_p, we first separate the measured temperatures into contributions from background and GW-induced perturbations. We accomplish that as follows. In a first step, a temperature background $\bar{T}$ is subtracted from the temperature measurements to obtain a sub-seasonal temperature perturbation T'. The background is assumed to comprise seasonal oscillations and is thus derived by applying a harmonic fit including annual and semiannual periods to the temperature profiles at each altitude in steps of 100 m (see Appendix A). The resulting $\bar{T}$ is illustrated in Figure A1. Figure 3a shows the retrieved sub-seasonal temperature perturbations. Signatures within T' comprise planetary waves (PW), tides, GWs, and other phenomena like sudden stratospheric warmings (SSW) or mesospheric inversion layers. In addition, we plot zonal wind contour lines over T'. The zonal winds are ERA5 data taken from the European Center for Medium-Range Weather Forecasts (ECMWF) and are spectrally truncated at wavenumber T21 to remove the influence of small-scale disturbances like GWs. For illustration reasons, we applied a running mean filter to the zonal winds with a width of 10 days and 5 km in time and the vertical, respectively. Clearly, strong temperature disturbances are visible in the winter months, and also a particularly large perturbation is found in mid-August 2019 just before the extraordinary SH SSW of 2019 occurred (e.g., Dörnbrack et al., 2020; Rapp et al., 2021, and references therein). In order to remove structures other than GWs from T' another filtering step is needed. A suitable

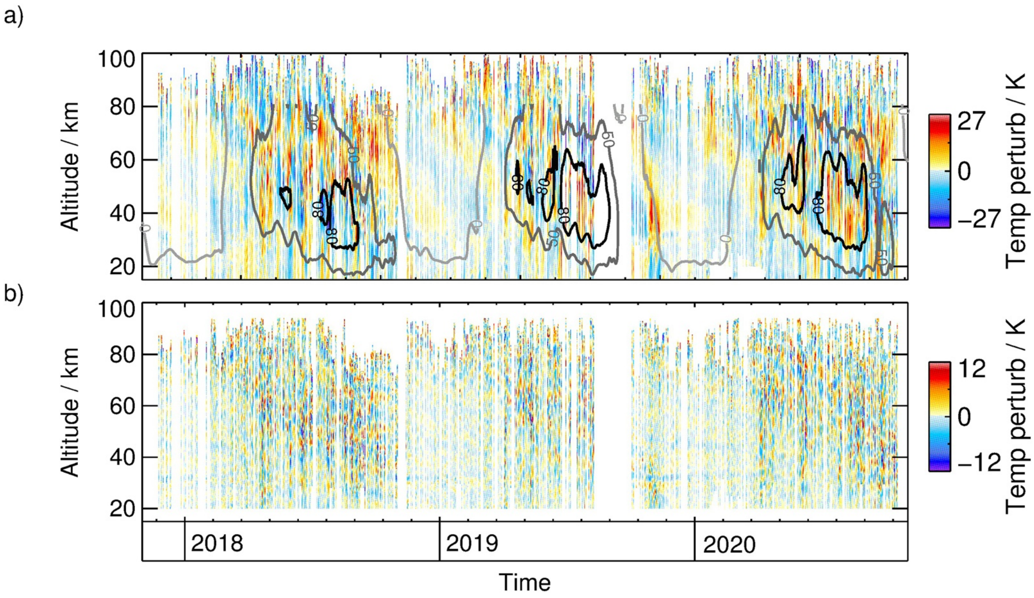

Figure 3. (a) Sub-seasonal temperature perturbations T' and (b) temperature perturbations $\tilde{T}$ with vertical wavelengths <15 km. The color scales cover 3σ of the distributions. Contour lines (0ms^{-1}, 50ms^{-1}, 80ms^{-1}) indicate the zonal wind taken from ECMWF.

way is the application of a fifth order Butterworth high-pass filter on vertical temperature profiles (Ehard et al., 2015). A critical parameter is the cutoff wavelength λ_{cut}. If chosen too small, a larger part of the GW spectrum will be assigned to the background. If chosen too large, background features like tides and PWs are taken for GWs. For the following analysis the cutoff wavelength is defined as $\lambda_{\text{cut}} = 15\,\text{km}$, a value used in multiple studies (Baumgarten et al., 2017; Bramberger et al., 2017; Kaifler et al., 2017; Rapp et al., 2018; Strelnikova et al., 2021). Given that seasonal oscillations exhibit vertical scales in the order of ∼70 km, the prior subtraction of them has a negligible effect on the scale separation of the Butterworth filter.

Please note that the Butterworth transfer function exhibits no sharp cutoff at λ_{cut} but dampens spectral amplitudes continuously for $\lambda_z > \lambda_{\text{cut}}$, that is, the output may still contain vertical structures larger than λ_{cut} but the amplitudes are very much reduced. The division of the temperature into background T_{BG} and perturbation $\tilde{T}$ is thus done in two steps and is given by

$$T = \bar{T} + T' \tag{2}$$

$$T = \bar{T} + \underbrace{T'' + \tilde{T}}_{} \tag{3}$$

$$T = T_{\text{BG}} + \tilde{T} \tag{4}$$

where T'' indicates perturbations with vertical wavelengths >15 km and $\tilde{T}$ perturbations with vertical wavelength <15 km. $\tilde{T}$ is illustrated in Figure 3b.

From Figure 3, it is evident that the Butterworth high-pass filter reduces maximum temperature amplitudes by a factor of two to three. Still, we detect strong disturbances in the winter months, whose envelopes follow roughly the zonal wind contour lines. But, enhanced amplitudes also occur in the summer mesosphere.

The buoyancy frequency is determined in the following way:

$$N = \sqrt{\frac{g}{T_{\text{BG}}}\left(\frac{dT_{\text{BG}}}{dz} + \frac{g}{c_p}\right)}, \tag{5}$$

where c_p is the heat capacity of dry air at constant pressure. The overbar in Equation 1 denotes that E_{p} is averaged over one cycle of a GW, that is, in case of lidar measurements one period and one vertical wavelength. Following Whiteway and Carswell (1995), we define the mean-square relative temperature perturbation as

$$\overline{\left(\frac{\tilde{T}}{T_{\mathrm{BG}}}\right)^2_{kl}} = \frac{1}{n_t n_z}\sum_{i=k-\frac{n_t}{2}}^{k+\frac{n_t}{2}}\ \sum_{j=l-\frac{n_z}{2}}^{l+\frac{n_z}{2}}\left(\frac{\tilde{T}}{T_{\mathrm{BG}}}\right)^2_{ij} \tag{6}$$

where k and l denote the discrete location in time and altitude at which the evaluation is done. The indices i and j run over the averaging window containing n_t and n_z lidar temperature observations where $\Delta t = n_t \cdot dt = 3$ h and $\Delta z = n_z \cdot dz = 15$ km with $dz = 100$ m and $dt = 15$ min in the vertical and time, respectively. The value of Δz is chosen in accordance to λ_{cut} and Δt is chosen in accordance to the required minimum measurement duration. In addition, we require that at least 90% of the averaging window is filled with data. The arithmetic mean E_{p} (represented in the following by $\diamond$) is computed as

$$\langle E_{\mathrm{p}}\rangle^{\diamond}_{kl} = \frac{1}{n_t n_z}\sum_{i=k-\frac{n_t}{2}}^{k+\frac{n_t}{2}}\ \sum_{j=l-\frac{n_z}{2}}^{l+\frac{n_z}{2}} E_{\mathrm{p},ij}. \tag{7}$$

For instance Baumgaertner and McDonald (2007) have shown that the E_{p} distribution follows a lognormal distribution taking into account 6 months of data. Hence, to describe the average E_{p} over long time scales, that is, months or years, we compute the geometric mean E_{p} (represented in the following by $\circledcirc$) as

$$\langle E_{\mathrm{p}}\rangle^{\circledcirc}_{kl} = \exp\left(\frac{1}{n_t n_z}\sum_{i=k-\frac{n_t}{2}}^{k+\frac{n_t}{2}}\ \sum_{j=l-\frac{n_z}{2}}^{l+\frac{n_z}{2}} \ln(E_{\mathrm{p},ij})\right). \tag{8}$$

In addition, the standard deviation and the skewness of the lognormal distribution is determined according to

$$\sigma^{\circledcirc}_{kl} = \sqrt{\frac{1}{n_t n_z}\sum_{i=k-\frac{n_t}{2}}^{k+\frac{n_t}{2}}\ \sum_{j=l-\frac{n_z}{2}}^{l+\frac{n_z}{2}}\left(\ln(E_{\mathrm{p},ij}) - \ln\left(\overline{E_{\mathrm{p},kl}}^{\circledcirc}\right)\right)^2} \tag{9}$$

and

$$\gamma^{\circledcirc}_{kl} = \frac{1}{n_t n_z}\sum_{i=k-\frac{n_t}{2}}^{k+\frac{n_t}{2}}\ \sum_{j=l-\frac{n_z}{2}}^{l+\frac{n_z}{2}}\left(\ln(E_{\mathrm{p},ij}) - \ln\left(\overline{E_{\mathrm{p},kl}}^{\circledcirc}\right)\right)^3. \tag{10}$$

Skewness provides information on whether the distribution is inclined toward large or low energy densities. Therefore, it also offers details about the GW intermittency. According to Plougonven et al. (2013), a reliable measure for the GW intermittency is the Gini coefficient. It is defined as

$$I_{\mathrm{g}} = \frac{\sum_{i=1}^{n-1}\left(i\,\overline{E_{\mathrm{p}}}^{\diamond} - \mathbb{E}_{\mathrm{p},i}\right)}{\sum_{i=1}^{n-1} i\,\overline{E_{\mathrm{p}}}^{\diamond}} \tag{11}$$

where $\mathbb{E}_{\mathrm{p}}$ is the cumulative sum over E_{p} values sorted in ascending order and $n = n_t n_z$ is the number of those E_{p} values that are included in the cumulative sum. Table 2 lists $\sigma^{\circledcirc}$, $\gamma^{\circledcirc}$, and I_{g} for four altitude regions and summer and winter separately. Calculations of the respective uncertainties are given in Appendix C.

3.2. Conservative Growth Curves

Previous studies compared their E_{p} profiles with the conservative growth rate (e.g., Alexander et al., 2011; Chu et al., 2018; Kaifler, Lübken, et al., 2015; Mzé et al., 2014; Wright et al., 2016). It was used to approximate the growth of potential energies due to the decrease of air density. The conservative growth rate is given as

Table 2

List of Geometric Mean Summer (Nov–Feb) and Winter (Apr–Sep) Potential Energies per Mass $\langle E_\mathrm{p}\rangle^{\circledcirc}$ *for Four Altitude Levels*

Altitude	20–35 km	35–50 km	50–65 km	65–80 km
$\langle E_\mathrm{p}\rangle^{\circledcirc}$	$2.8 \mathrm{Jkg}^{-1}$	$2.8 \mathrm{Jkg}^{-1}$	$5.8 \mathrm{Jkg}^{-1}$	$31.4 \mathrm{Jkg}^{-1}$
	$8.2 \mathrm{Jkg}^{-1}$	$21.1 \mathrm{Jkg}^{-1}$	$58.6 \mathrm{Jkg}^{-1}$	$82.4 \mathrm{Jkg}^{-1}$
$\sigma^{\circledcirc}$	0.66	0.52	0.61	0.81
	0.88	0.96	0.75	0.58
$\gamma^{\circledcirc}$	0.19	0.01	0.06	0.00
	0.28	0.27	−0.02	0.02
I_g	0.33	0.23	0.22	0.25
	0.43	0.44	0.37	0.22
Sample size	148 h	234 h	323 h	272 h
	1,993 h	2247 h	2335 h	1,941 h

Note. $\sigma^{\circledcirc}$ repesents the geometric standard deviation, $\gamma^{\circledcirc}$ the skewness of the lognormal E_p distribution, and I_g the Gini coefficient. Gray shading marks winter values

$E_\mathrm{p}(z) = E_0 \exp\left(\frac{z}{H_\mathrm{s}}\right)$ where E_0 is an initial amplitude. The scale height H_s was either determined from an average temperature (Alexander et al., 2011; Kaifler, Lübken, et al., 2015; Mzé et al., 2014; Wright et al., 2016) or was fitted to the E_p profiles (Chu et al., 2018), but it was always considered to be constant with height. As H_s changes significantly with temperature and therefore with altitude, we compare our derived E_p profiles with conservative growth curves that are a function of temperature. The implications are discussed in Section 5.4. The scale height $H_\mathrm{s}(z) = \frac{RT(z)}{Mg}$ is calculated using the monthly mean temperature profiles shown in Figure 2. The symbol R is the universal gas constant and $M = 29.0\mathrm{g\ \ mol}^{-1}$ is the mean mass of 1 mol of the atmosphere.

3.3. WAVELET-SCAN

Vertical wavelengths of GWs generally vary in time as well as in altitude while interacting with the background wind field (e.g., Bühler, 2014; Marks & Eckermann, 1995). Besides, multiple waves can superimpose or even interact nonlinearly, leading to complex wave patterns in lidar temperature data. Although 1D wavelet analysis preserves the altitude information of spectral modes, lidar studies mostly focus only on dominant modes and neglect weaker ones (e.g., Baumgarten et al., 2017). We developed a new method that is based on 1D wavelet analysis but also keeps track of temporal and vertical changes of more than one coherent spectral mode by utilizing a clustering algorithm. We call this new method WAVELET-SCAN.

In a first step, a temperature profile is analyzed in the vertical using a continuous wavelet transform (Torrence & Compo, 1998). As mother wavelet we use the Morlet wavelet that is described as $\Psi_0(\eta) = \pi^{-1/4} e^{i\omega_0\eta} e^{-\eta^2/2}$, where ω_0 is the nondimensional frequency and η the nondimensional time. We set $\omega_0 = 4$ to fulfill the admissibility condition, that is, the integral over the wavelet is zero. Input scales are defined as $s_j = \Delta z \cdot 2^{j/8+1}$ with $\Delta z = 1.0$ km and output scales, that is, vertical wavelengths, are interpolated onto a linear grid. The results of the CWT are spectral amplitudes as function of altitude and vertical wavelength $W_z(\lambda_z)$. We determine the underlying structure or "skeleton" (Torrésani, 1995) by identifying local maxima in spectral amplitude in the direction of vertical wavelength, that is, a zero-crossing from positive to negative values in $\frac{\partial W_z}{\partial \lambda_z}$. This step is repeated for all consecutive temperature profiles obtained in one measurement night and yields first $W_{t,z}(\lambda_z)$ and second a "skeleton" in the t-z-λ_z-space. In addition we require $W_{t,z}(\lambda_z) > 3.0\ \ \mathrm{K}$ and $W_{t,z}(\lambda_z) > \frac{\Delta T}{2}$ in order to minimize the contribution by tides and measurement uncertainties. We illustrate the derivation of the "skeleton" in Figure 4. Figure 4e shows an example of sub-seasonal temperature perturbations T' on the night from June 18 to 19, 2018. Clearly, large-amplitude waves were observed at this date. As described above, we apply CWTs to all vertical profiles and subsequently average $W_{t,z}(\lambda_z)$ to illustrate the three-dimensional structure. In Figures 4a and 4c, we average $W_{t,z}(\lambda_z)$ between 55 and 95 km and between 15 and 55 km, respectively. The same holds true for Figures 4b and 4d. Here, we average $W_{t,z}(\lambda_z)$

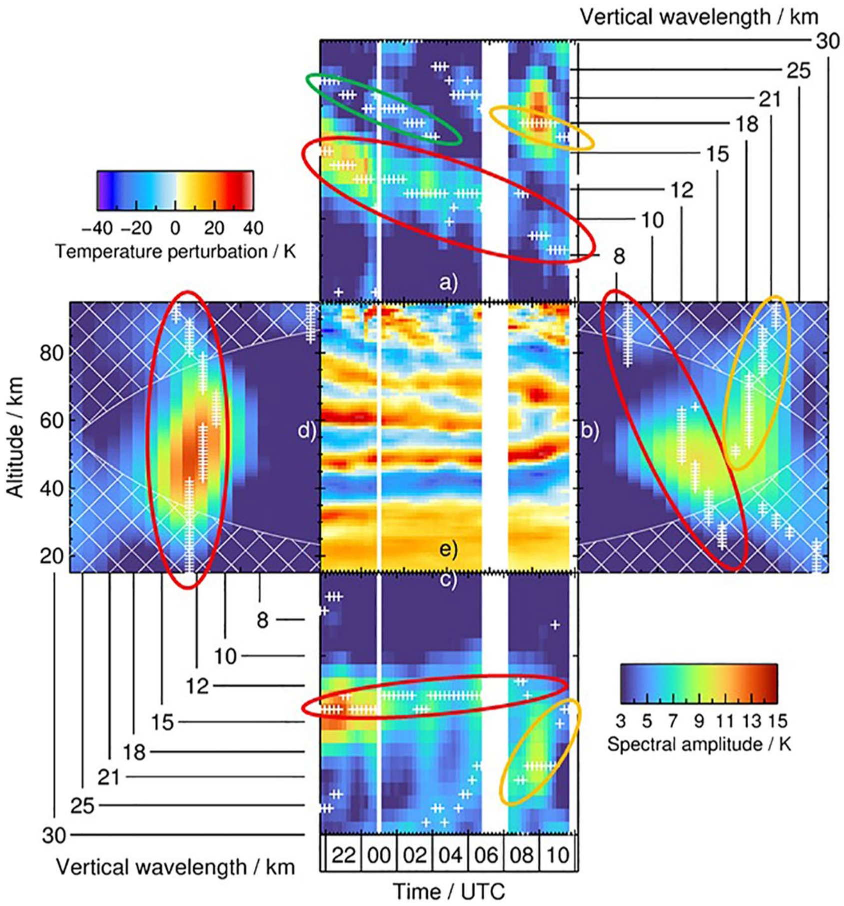

Figure 4. Wavelet spectrum averaged over altitudes 55–95 km (a) and altitudes 15–55 km (c) and averaged from 22 UTC to 05 UTC (d) and from 05 UTC to 12 UTC (b). Sub-seasonal temperature perturbations T' on June 18–19, 2018 are shown in (e). The hatched areas mark the cone of influence. White crosses mark local maxima in spectral amplitude. The red, green, and orange ellipses highlight wave packets I–III, IV, and V respectively.

over the first half of the night (22 UTC–05 UTC), and the second half of the night (05 UTC–12 UTC), respectively. With this arrangement, we illustrate the walls of the box representing $W_{t,z}(\lambda_z)$ and get a good insight into its structure. The white crosses mark the positions of local maxima in $W_{t,z}(\lambda_z)$.

Multiple maxima exist for $W_{t,z}(\lambda_z)$ and ultimately form hypersurfaces in (z, t, λ_z). The challenge is to identify those hypersurfaces which represent in physical space wave packets that exhibit varying vertical wavelengths in time and altitude. We solved this problem by implementing a clustering algorithm as the second step of WAVELET-SCAN.

The Density-Based Spatial Clustering of Applications with Noise (DBSCAN) is able to separate densely packed data points with many nearby neighbors from isolated outliers (Ester et al., 1996). The critical value that has to be defined is the data point density. It is defined as the minimum number of points, $minPts$, that must be within a neighborhood of radius ε of any point. Normalizing by Δt, Δz, and $\Delta\lambda_z$, we represent the t-z-λ_z-space as a Cartesian grid with unit distance $\varepsilon = 1$. As the data points represent maxima in the λ_z-direction, the minimum distance between two adjacent maxima in that direction is $\varepsilon = 2$. To ensure that we identify only one λ_z for each time and altitude, we choose $\varepsilon = \sqrt{2}$ and in addition $minPts = 7$. These settings turn out best for our purposes and result in a sufficient identification of coherent wave packets. For further details on the functionality of the DBSCAN, we refer to Ester et al. (1996).

After a wave packet is identified, we require that its temporal and vertical extent is larger than 3 h and larger than the average vertical wavelength, respectively. By that, we ensure that the packet encloses at least one full oscillation in the vertical.

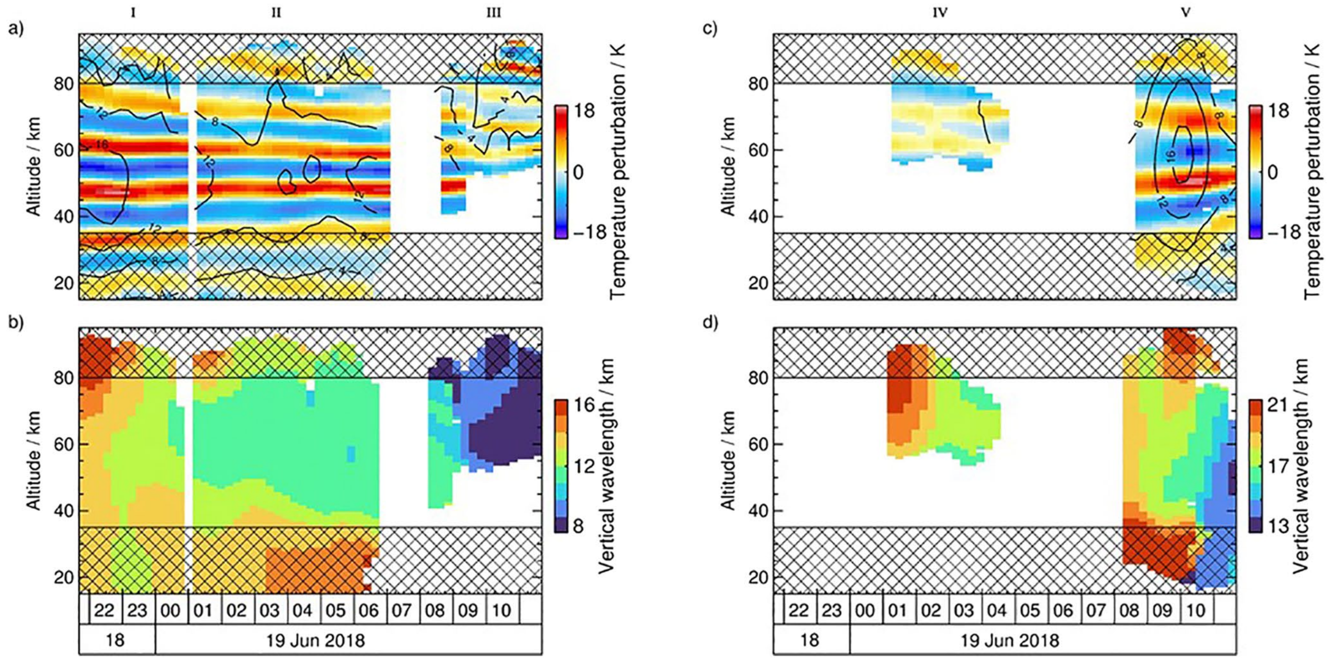

Figure 5. Analysis of the measurements on June 18–19, 2018 shown in Figure 4e based on WAVELET-SCAN: (a) reconstructed wave packets with contour lines indicating spectral amplitudes, (b) derived vertical wavelength of wave packets I – III. Panels (c) and (d) display the same as (a) and (b) but for wave packets IV and V. Hatched areas mark the COI. Please note different λ_z-ranges for (b) and (d).

To demonstrate its capabilities we applied WAVELET-SCAN to artificial temperature data (see Appendix B) as well as to consecutive T'-profiles that were obtained on the night from June 18–19, 2018. The output is a number of wave packets that represent multiple coherent spectral modes. For each wave packet, vertical wavelengths, spectral amplitudes, and the cone of influence (COI) are retrieved. The COI describes the part of the wavelet spectrum where the determined spectral amplitudes are generally underestimated due to edge effects and are thus less reliable.

The sub-seasonal temperature perturbations (Figure 4e) belong to a series of measurements that were conducted between June 16 and June 23, 2018. In that period of time the mean vertical wavelength is 16 km (N. Kaifler et al., 2020). The spectral analysis of T' on June 18–19, 2018 performed by WAVELET-SCAN reveals more details. Superimposed coherent wave packets are revealed by the distributions of vertical wavelengths and by the reconstructions (Figures 5a–5d). The first packet extends over the whole altitude range and measurement duration. WAVELET-SCAN actually identifies three packets (I–III) separated by two measurement gaps, but as the reconstructed wave patterns demonstrate, the three identified packets belong to one single wave packet. This wave packet also causes the largest spectral amplitudes in the wavelet spectra (see red ellipses in Figures 4a, 4c, and 4d). Its average vertical wavelength is 12 km at the beginning of the measurement and the spectral amplitude starts with about 17 K. With progressing time, the vertical wavelength shrinks to 9–10 km and the amplitude decreases as well to about 10 K until ∼0700 UTC. At 0900 UTC, the wave packet is limited to altitudes above 50 km and exhibits significantly smaller vertical wavelengths on the order of 6 km. That first wave packet dominates T' and is linked to a strong mountain wave event (Kaifler et al., 2020). Please note that spectral amplitudes in Figures 4a–4d and 5a and 5c are systematically underestimated. This is due to the fact that the variance of the signal is distributed over several scales because in contrast to a pure sin-function, the wavelet is spectrally broad. But, as only one scale is reconstructed, the variance of the reconstructed signal is smaller than the variance of the input signal. It is unclear whether the last two packets (IV and V) are actually parts of one single wave packet that is divided by the measurement gap. But, both packets show similar vertical wavelengths and hence we show them next to each other. Wave packet IV (see green ellipse in Figure 4a) appears between 0100 UTC and 0430 UTC in the altitude range 55–90 km. It has a vertical wavelength of 16–18 km and spectral amplitudes below 4 K. After the second measurement gap, we notice wave packet V (see orange ellipses in Figures 4a–4c) spanning the total altitude range with vertical wavelengths of 17 km decreasing to 11 km within three hours. Its largest spectral amplitude is 17 K.

The vertical wavelength of linear hydrostatic MWs can be considerably larger than λ_{cut} as evident from the approximation $\lambda_z = 2\pi \frac{u}{N}$ (Nappo, 2002). For example, assuming a westerly wind of $70\mathrm{ms}^{-1}$ and a stratospheric $N = 0.02\mathrm{s}^{-1}$ results in $\lambda_z = 22$ km in case of a westward propagating wave. Also, the extreme wave profiles in Figure 2 indicate vertical wavelengths in the order of 20 km. Therefore, we apply WAVELET-SCAN not to $\tilde{T}$ but to T' in order to be sensitive to GWs with vertical wavelengths larger than λ_{cut}.

3.4. 2D Kernel Density Estimation

Retrieved vertical wavelengths Λ are associated with the time and altitude Z of their occurrence. The incidence of waves as function of vertical wavelength and altitude is determined by means of a two-dimensional KDE. We follow Rosenblatt (1956) and Parzen (1962) and define the kernel density estimator as

$$\hat{f}(z, \lambda; h) = \frac{1}{n} \sum_{i=1}^{n} K_h(z - Z_i, \quad \lambda - \Lambda_i) \tag{12}$$

where we extend their approach to two dimensions. As Kernel K_h, we use a two-dimensional Gaussian distribution, which is given as

$$K_{h_z h_\lambda}(z, \lambda) = \frac{1}{2\pi h_z h_\lambda} \exp\left(-\frac{1}{2}\left(\left(\frac{z}{h_z}\right)^2 + \left(\frac{\lambda}{h_\lambda}\right)^2\right)\right) \tag{13}$$

where h_z and h_λ are called bandwidths and represent the standard deviation of the Gaussian distribution. In this case, we use the bandwidths $h_z = h_\lambda = 1.0$ km. Both values represent the vertical temperature resolution. The number of (Z, Λ)-pairs is given by n.

3.5. 2D Wavelet Analysis

The 2D Morlet wavelet used in the analysis is characterized by two parameters: the angle θ defines the direction of the wave vector in t-z-space and the scale s corresponds to the period along this direction. θ is defined anti-clockwise, where $\theta = 90°$ represents a wavelet with stationary phaselines. Other orientations can be converted into vertical phase speeds c_z according to $c_z = \frac{\Delta z}{\Delta t}\tan\theta$ where Δz and Δt represent the resolution of the data grid. Following the work by Zhao et al. (2017), we chose $c_z = \pm[0.0, 0.4, 0.7, 1.0, 1.3]\mathrm{ms}^{-1}$ to detect steady ($c_z = 0$), apparently upward ($c_z > 0$) and downward propagating ($c_z < 0$) waves. Kaifler et al. (2017) used the criterion $c_z < -0.35\mathrm{ms}^{-1}$ for downward and $c_z > 0.35\mathrm{ms}^{-1}$ for upward propagating waves. The scale s is chosen as suggested by Torrence and Compo (1998) such that, in case of MWs, vertical wavelengths from 2 to 15 km are covered. Naturally, λ_z increases for a phaseline pattern with constant spacing when the orientation deviates from 90°, that is, for up- and downward propagating waves. Hence, we truncate s as function of θ in order to guarantee a maximum vertical wavelength of 15 km. We proceeded with our analysis as follows. One wavelet transformation is performed for each combination (θ, s). After that, temperature perturbations are reconstructed separately and averaged over orientations of associated wave classes. Finally, we compute the RMS of the temperature reconstructions of each wave class over four altitude regions and the duration of the measurement. The altitude regions are the same as in Section 4.1 and represent the lower and upper stratosphere as well as the lower and upper mesosphere. The analysis is applied to each measurement lasting at least 6 h, that is, we focus on the winter season, as measurements in summer are generally shorter. The total winter RMS is derived by integrating the RMS values over all measurements, the four altitude regions and the three wave classes. We derive the contribution of each wave class by integrating the RMS values over all measurements as well as one altitude range and one wave class of interest and dividing the result by the total winter RMS.

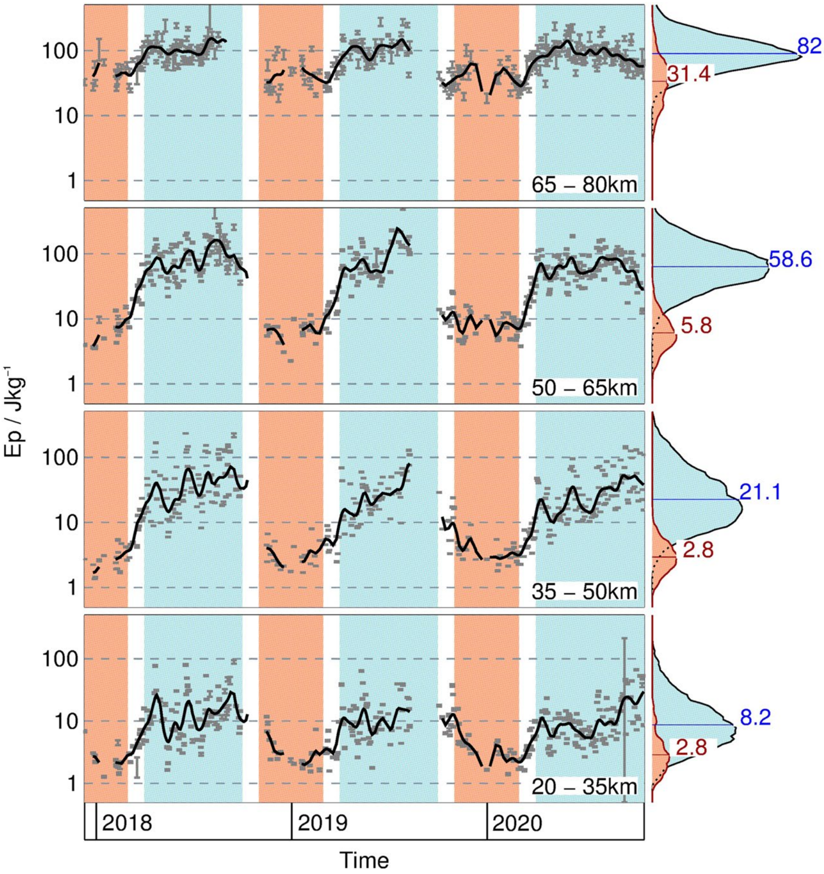

Figure 6. Time series of $\langle E_p \rangle^\diamond$ for four different altitude regions. The black line represents $\langle E_p \rangle^\diamond$ filtered with a 30-day Hann filter. Histograms represent wintertime (blue) and summertime (red) E_p distributions. The horizontal blue and red lines mark the geometric averages of the distributions. Please note the logarithmic y-axis, which is also valid for the histograms. See text for details.

4. Results

First, we focus on the temporal as well as vertical distribution of GW potential energy per mass. Also, statistical parameters like skewnesses and Gini coefficients are listed for different altitude regions. Second, results of our spectral analysis are presented, including the investigation of stationary phaselines and WAVELET-SCAN.

4.1. Seasonal Variation in GW Potential Energy

We now present the results of the analysis of GW potential energies. Please have in mind that the $\diamond$ symbol represents a short-term arithmetic average, typically over the duration of a measurement night, while the $\odot$ symbol represents a long-term geometric average over months or years. Figure 6 shows $\langle E_p \rangle^\diamond$ averaged over a Δt that is at least 3 h and at maximum equal to the duration of each individual night, and the following four altitude regions: 20–35 km (lower stratosphere), 35–50 km (upper stratosphere), 50–65 km (lower mesosphere), and 65–80 km (upper mesosphere). To guide the eye, a curve representing the data filtered by a 30-day Hann filter is superimposed. The colored areas in the background mark winter (April–September) and summer months (November–February). White areas represent transition months from summer to winter (March) and vice versa (October). Averages as well as standard deviations and skewnesses of lognormal E_p distributions for the four altitude regions are compiled in Table 2. In addition, sample sizes and Gini coefficients are listed.

The $\langle E_\mathrm{p}\rangle^\diamond$ time series presented in Figure 6 show a pronounced annual variation at all altitudes with a minimum in austral summer and a maximum in winter. The largest difference between the summer and winter $\langle E_\mathrm{p}\rangle^\circledcirc$ is found in the lower mesosphere. Here, potential energies are about 10 times larger in winter than in summer (Table 2). In the upper mesosphere, a semiannual variation with a narrow peak in summer and a broad peak in winter can be identified. The minima of this semiannual variation coincide with the transition months March and October. A semiannual variation in zonal wind variances was also observed at Andenes and Juliusruh (Hoffmann et al., 2010). Striking are several high-energy events, exceeding $100 \mathrm{Jkg}^{-1}$ already in the upper stratosphere. While this was only twice the case in 2019 and happened four times in 2020, in 2018 we find these events more frequently (e.g., Kaifler et al., 2020). It is worth mentioning that November, although classified as summer month, exhibits winter-like energies in the lower stratosphere. This results in relatively large values for $\sigma^\circledcirc$, $\gamma^\circledcirc$ and the Gini coefficient for the summer lower stratosphere (Table 2). In addition, histograms for summer and winter are shown to the right of each time series with thin horizontal lines indicating geometric averages. Drawn on a logarithmic axis, the histograms appear roughly as a normal distribution. This was already observed for GW potential energies (Baumgaertner & McDonald, 2007; Chu et al., 2018; Kaifler, Lübken, et al., 2015; Mzé et al., 2014) and for GW momentum fluxes (Hertzog et al., 2012). In the lower and upper stratosphere, histograms exhibit tails toward larger E_p values in winter, reflecting enhanced GW intermittency.

4.2. Potential Energy as Function of Altitude

We next look at monthly mean $\langle E_\mathrm{p}\rangle^\circledcirc$ profiles in which we consider E_p values that fall into the respective month (see Figure 7). Profiles are truncated in altitude if the number of data points at a given altitude is below 50% of the maximum number of data points.

We initialize conservative growth curves with $E_0 = (1, 2, 5) \times (10^{-3}, 10^{-2}, 10^{-1}, 10^{0})\ \mathrm{Jkg}^{-1}$ at 15 km and show them together with our derived $\langle E_\mathrm{p}\rangle^\circledcirc$ profiles in Figure 7. In analogy to Figure 2, we show one extreme energy profile for each month to highlight the extraordinary wave amplitudes and the resulting variability in $\langle E_\mathrm{p}\rangle^\circledcirc$ profiles. Please note that the selected extreme profiles in Figures 2 and 7 do not necessarily refer to the same measurement nights because extreme temperature amplitudes may be damped in the E_p analysis, if the λ_z associated with the temperature perturbation is larger than λ_cut.

In summer, $\langle E_\mathrm{p}\rangle^\circledcirc$ profiles do not differ substantially from month to month. Low energies as well as small standard deviations are observed from 20 up to 60 km. Increased energies accompanied by larger standard deviations are only found in the lower stratosphere in November. Above 60 km, $\langle E_\mathrm{p}\rangle^\circledcirc$ increases rapidly and eventually reaches a maximum at ∼80 km. In contrast to the stratosphere, where observed energies are growing at a slower rate than the conservative growth rate, summer $\langle E_\mathrm{p}\rangle^\circledcirc$ profiles become closer aligned to the sketched conservative growth curves in the mesosphere. In summer, we notice generally smaller conservative growth rates in the stratosphere than in the mesosphere. In March, initial energies in the lower stratosphere are comparable to summer months but exhibit larger standard deviations. In winter, all $\langle E_\mathrm{p}\rangle^\circledcirc$ profiles show significant growth up to ∼60 km and level off above. Winter profiles also have large standard deviations in common that extend from the lower stratosphere up to the lower mesosphere with summer-like standard deviations in the upper mesosphere. Energies grow moderately from 20 km up to ∼40 km in April and May and exhibit a remarkable $\langle E_\mathrm{p}\rangle^\circledcirc$ increase up to 60 km. Between 40 and 60 km, the $\langle E_\mathrm{p}\rangle^\circledcirc$ profile and the conservative growth curves are very much aligned in May. This zone with approximately conservative growth rates persists until September and extends further down covering the height range from 30 km up to 50 km. In winter, the altitude range ∼30–50 km shows noticeable smaller conservative growth rates than below and above. In October, $\langle E_\mathrm{p}\rangle^\circledcirc$ grows up to 40 km similar to winter months but reaches a local minimum at 55 km, only to grow above again. In the same time E_p geometric standard deviations are exceptionally large in the upper stratosphere.

The extreme energy profiles shown in Figure 7 suggest that individual wave events can lead to E_p values that are five times larger than the monthly average in summer and up to 10 times larger in winter. Remarkable is the extreme energy profile in April when $E_\mathrm{p} > 50 \mathrm{J\ kg}^{-1}$ over the entire altitude range and even $>100 \mathrm{J\ kg}^{-1}$ from 30 km to over 80 km. In May and June, we find that potential energies do not always increase monotonically. The anomalous maximum potential energy at about 60 km demonstrates what happens when a

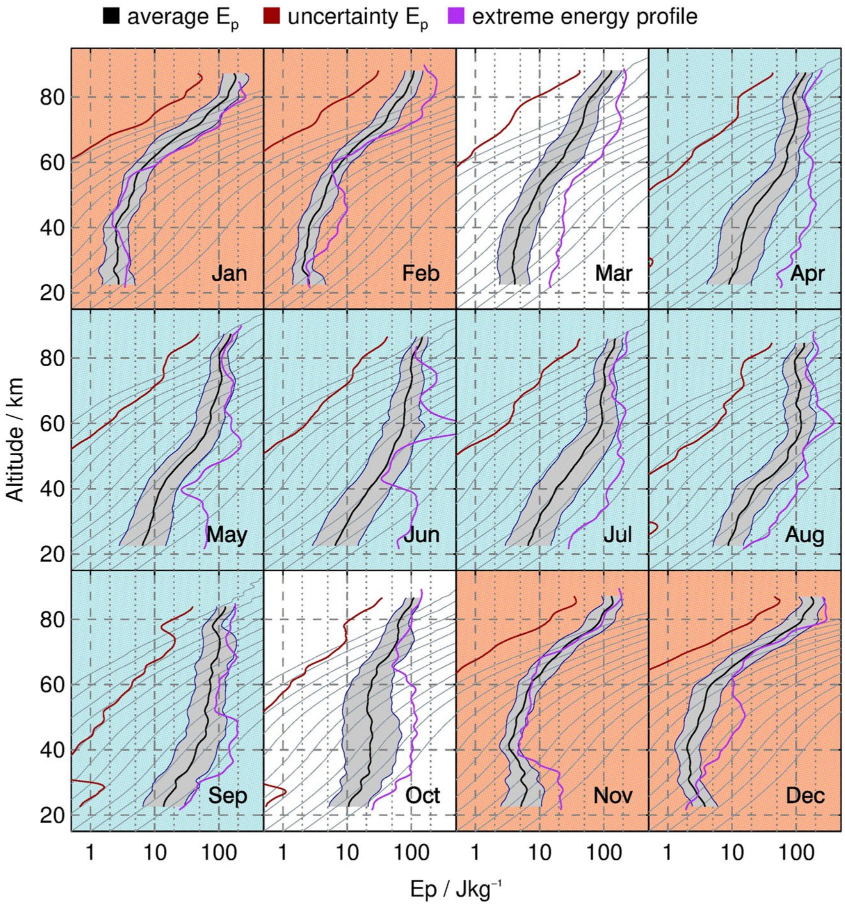

Figure 7. Profiles of monthly averaged gravity wave (GW) potential energy $\langle E_\mathrm{p}\rangle^{\circledcirc}$ (black), monthly averaged E_p uncertainty (red), and nightly extreme values (purple). The shaded area indicates the geometric standard deviation of E_p values and the gray hairlines mark conservative growth curves $\sim \exp(z/H_s(z))$. Dashed lines mark the following intervals: 2, 5, 20, 50, and 200Jkg^{-1}. Background colors indicate SH summer (red) and winter (blue). See text for details.

large-amplitude wave with $\lambda_z > 15$ km is incorrectly assumed to be part of the background in the energy analysis. A very large negative temperature gradient leads to a very low buoyancy frequency at that altitude, which results in E_p taking on very large values. In September, the extreme energy profile indicates growth rates larger than the conservative growth rate in the lower stratosphere.

4.3. Spectral Analysis of Sub-seasonal Temperature Perturbations

The sub-seasonal temperature perturbations T' contain signatures of PWs, tides, and GWs. PWs have significantly larger vertical wavelengths than GWs and, if detected, will only appear in the COI. Therefore, we focus this discussion on the results outside the COI. To be less sensitive to tides we required a minimum spectral amplitude of 3 K. We applied WAVELET-SCAN to winter measurements spanning more than 3 h and 60 km in time and altitude, respectively. The KDE based on all detected wave packets is illustrated in Figure 8 with the hatched area indicating the COI.

We find wave packets at all altitudes and with vertical wavelengths between 5 and 30 km. The maximum of the KDE is between 10 and 16 km vertical wavelength and in the altitude range 45–80 km. When we integrate the PDF over the entire height range and from 4 to 15 km of vertical wavelengths we get 42%. A probability of 50% is retrieved when we integrate the PDF up to 16.5 km vertical wavelength. Wave packets exhibiting vertical wavelengths >20 km appear in 35% of the cases.

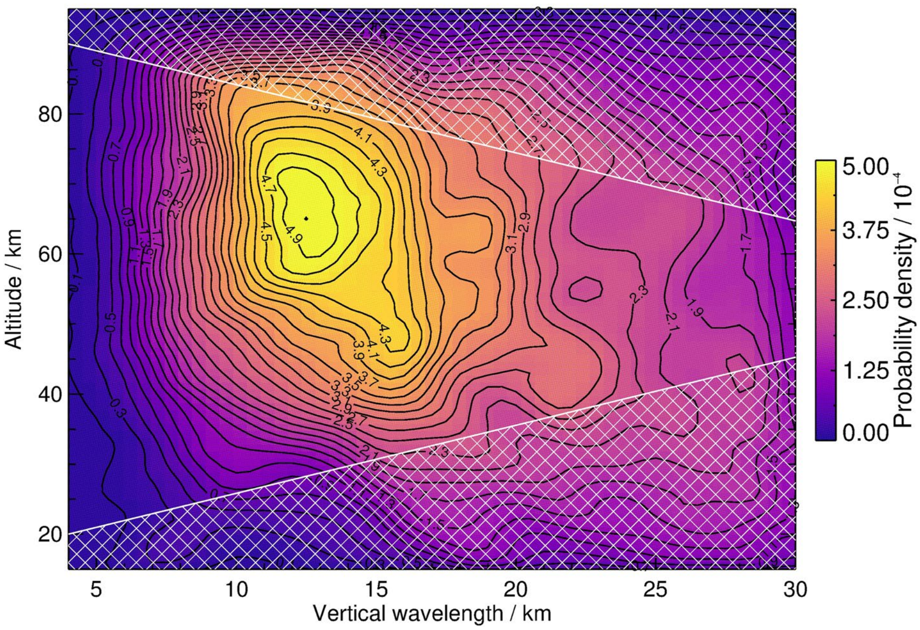

Figure 8. Two-dimensional kernel density estimation (KDE) as function of vertical wavelength and altitude. The white hatched area marks the cone of influence (COI). Only data obtained between April and September of 2018, 2019, and 2020 are incorporated.

4.4. Identification of Stationary as well as Apparently Up- and Downward Propagating Waves

We analyzed the wave patterns in temperature data by means of two-dimensional wavelet analysis (Chen & Chu, 2017; Kaifler, Kaifler, et al., 2015; Kaifler et al., 2017) and sorted GW-induced temperature perturbations into three wave classes depending on the angle of the phase lines in time-height cross sections (t-z-space). The three wave classes comprise apparently upward propagating waves, stationary waves, and apparently downward propagating waves. Dörnbrack et al. (2017) have shown that the relation of the background wind to the wave's group speed plays a major role in how GWs appear in lidar data. For simplicity and lack of measured wind data, we only distinguish between apparently up- and downward propagating waves and do not account for potential Doppler shifts, which can reverse the sign of the slope of phase lines in t-z-cross sections. Table 3 lists the contributions to the total winter RMS of temperature reconstructions for each wave class in the four altitude regions.

Stationary MWs account for slightly more than 50% of sub-seasonal temperature perturbations at all altitudes. Their contribution increases up to the lower mesosphere. Apparently, up- and downward propagating waves find their maximum contribution in the upper and lower mesosphere, respectively. Kaifler et al. (2017) also discovered largest wavelet power for MWs and a larger number of apparently up- than downward propagating waves.

Table 3
Contributions of Steady as Well as Apparently Up- and Downward Propagating Waves to the Total Winter RMS of Temperature Reconstructions

Altitude range (km)	Steady	Upward propagating	Downward propagating	Total
65–80	16.0%	9.7%	6.0%	31.7%
50–65	17.2%	8.4%	6.7%	32.3%
35–50	12.9%	5.4%	5.0%	23.3%
20–35	7.3%	2.7%	2.7%	12.7%
20–80	53.4%	26.2%	20.4%	100.0%

5. Discussion

As demonstrated in Figure 1, CORAL acquired measurements on average in two thirds of all nights due to fully automatic operation and generally good weather conditions in the lee of the Southern Andes. This is an exceptionally high and so far unprecedented measurement cadence for a mesospheric lidar system (Kaifler & Kaifler, 2021). The high cadence allows for the investigation of GW events on time scales in the order of a few hours up to several days (Kaifler et al., 2020). The statistical analysis of the CORAL data set provides significant results on the temperature structure, GW intermittency, the distribution of potential energies, and vertical wavelengths at the Southern Andes GW hot spot.

5.1. Forcing of MWs and Propagation Conditions

We have shown in Section 4.4 that more than half of the sub-seasonal temperature perturbations are caused by quasi-steady T' phase lines indicating quasi-stationary MWs. However, Río Grande is at least 100 km away from the closest mountain peak. It is located on the east coast of Tierra del Fuego and surrounded in the west by the southern foothills of the Andes. Smaller mountains (~1,000 m peak altitude) are located in the south and west (one exception is Mt Darwin with a peak altitude of 2488 m at ~150 km distance) while higher mountain peaks (e.g., Mt. Fitz Roy with a peak altitude of 3,405 m at ~600 km distance) are far to the northwest. So where do the observed waves originate from assuming they are mountain waves? Surely, this question cannot be answered alone on the basis of CORAL data, as observations above a single point lack the required horizontal information. From linear wave theory, we know that depending on the waves' intrinsic frequencies their horizontal group speeds can be substantial. Queney (1948) and Gill (1982) define two hydrostatic wave regimes. The dispersion relation in the nonrotating or mid-frequency regime ($N \gg \hat{\omega} \gg f$) is given by

$$\hat{\omega} = N \left| \frac{k_{\mathrm{h}}}{m} \right| \tag{14}$$

where $\hat{\omega}$ is the intrinsic frequency, k_{h} is the horizontal wavenumber, and m is the vertical wavenumber. The intrinsic phase velocity in this regime is simply

$$c_{\mathrm{ph}} = -\frac{N}{m} = -u_{\mathrm{h}} \tag{15}$$

where we have assumed that $k_{\mathrm{h}} < 0$ because the MWs propagate against the prevailing wind, which is westward in winter in the Southern Andes region. The intrinsic group velocity is defined as

$$c_{\mathrm{gh}} = \frac{\partial \hat{\omega}}{\partial k_{\mathrm{h}}} = -u_{\mathrm{h}}. \tag{16}$$

It becomes evident that as phase velocity and group velocity are identical, hydrostatic waves in the nonrotating regime are not dispersive. They have rather small horizontal wavelengths (<100 km) and propagate merely vertically. In the rotating or low-frequency regime ($\hat{\omega} \sim f$) the dispersion relation is given by

$$\hat{\omega} = \sqrt{N^2 \frac{{k_{\mathrm{h}}}^2}{m^2} + f^2}. \tag{17}$$

The phase velocity is thus

$$c_{\mathrm{ph}} = -\sqrt{\frac{N^2}{m^2} + \frac{f^2}{k_{\mathrm{h}}^2}} \tag{18}$$

and the group velocity is given as

$$c_{\mathrm{gh}} = -\frac{N^2}{m^2 u_{\mathrm{h}}}. \tag{19}$$

In the rotating wave regime, we find $c_{\mathrm{ph}} \neq c_{\mathrm{gh}}$, which means that waves in this regime are dispersive. They have rather large horizontal wavelengths (>100 km) and propagate both in the vertical but also in the horizontal. As an illustration, we show in Figure 9 the topography of the Southern Andes and depict the two wave regimes above. The hydrostatic nonrotating waves appear right above the mountain peaks, for example above Mt. Darwin and Mt. Fitz Roy. These waves exhibit horizontal scales that are of the same order as their vertical scales as long as u and N remain constant. The further away their sources, the less likely it is to observe hydrostatic nonrotating waves above Río Grande. Waves in the hydrostatic rotating wave regime exhibit horizontal scales that are significantly larger than their vertical scales and originate from the envelope of the Southern Andes topography rather than from individual mountain peaks. These waves extend leeward of the mountains including over Río Grande where we can observe them with CORAL. The spreading of MWs leeward of the mountains was observed by Dörnbrack et al. (1999) in Scandinavia but

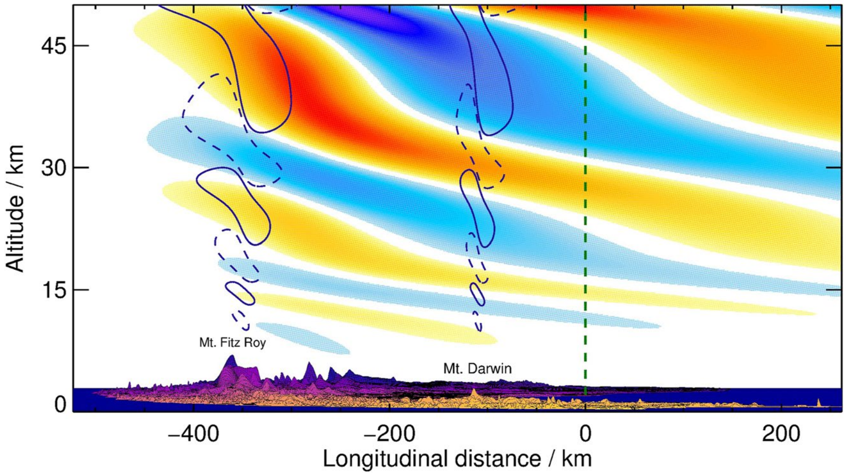

Figure 9. Depiction of mountain waves (MWs) above the Southern Andes. The orange-purple colormap indicates latitudinal distance of the topography and the red-blue colormap symbolizes the wavefield associated with hydrostatic rotating waves. Contour lines sketch wave fields associated with hydrostatic nonrotating waves. The green dashed line marks CORAL's laser beam.

is also reported for the Southern Andes region in publications by, for example, Jiang et al. (2013); Kaifler et al. (2020); Wright et al. (2017).

Let us now consider the forcing and propagation conditions. Figure 10 shows profiles of monthly mean wind speeds and directions at Río Grande taken from ECMWF. The ERA5 wind data were spectrally truncated at wavenumber T21 in order to filter out contributions from model-resolved GWs and obtain a smooth background wind field. First of all, there have to be sufficiently large tropospheric winds perpendicular to the mountain ridge for excitation of MWs (e.g., Bramberger et al., 2017; Dörnbrack et al., 1999; Kaifler, Kaifler, et al., 2015). In addition, Dörnbrack et al. (1999) report that good excitation conditions prevail when the wind turns no more than 30° within the first 30 km. Monthly mean wind speeds in ERA5 data are at about 15 ms^{-1} at surface level (500 m) at all times. The wind rotation within the first 30 km is <30° during the months from March to October with a surface level forcing between 240° and 280°. Thus, in the climatological mean MWs are excited and able to propagate deep into the middle atmosphere in the winter months. A strong wind rotation within the first 30 km of about 60° can only be observed in July 2020. At this time, we also find reduced GW energies at all altitude regions (see Figure 6). For upward propagation, the wind speed in the direction of wave propagation must not become zero as this would lead to wave breaking (Lindzen, 1981). Moreover, for deep vertical propagation, the MWs should not encounter turning levels where the intrinsic frequency approaches the buoyancy frequency (e.g., Schoeberl, 1985). These conditions occur in the core of the PNJ and filter horizontally short MWs or lead to evanescent modes tunneling through the PNJ (e.g., Mixa et al., 2021). Another obstacle for MWs is the stratospheric wind minimum where the waves' u'-amplitude may become equal to the horizontal wind speed causing wave breaking. This wind minimum can act as a valve for vertically propagating MWs (Kruse et al., 2016). Figure 10 reveals that low wind speeds at ~25 km altitude occur from March to May. In the winter months, with positive temperature gradients (Figure 2) and large horizontal wind speeds (Figure 10) up to 50 km, generally good vertical propagation conditions can be expected. Above, shear instabilities and unstable lapse rates lead to wave dissipation. On the other hand, the mesosphere is the favorable region for the generation of secondary gravity waves (Heale et al., 2020; Kogure et al., 2020; Vadas & Becker, 2019; Vadas et al., 2018). Large contributions of apparently up- and downward propagating waves and reduced contributions of stationary waves (see Table 3) at mesospheric altitudes might indicate their existence above Río Grande. In addition, apparently upward propagating waves detected in the mesosphere may have been convectively generated GWs from deep convection zones far in the north (Fritts & Alexander, 2003; Yuan et al., 2016; Yue et al., 2014). However, given the on average large group speed of convectively generated waves and the large horizontal distance to Río Grande, this does not seem likely.

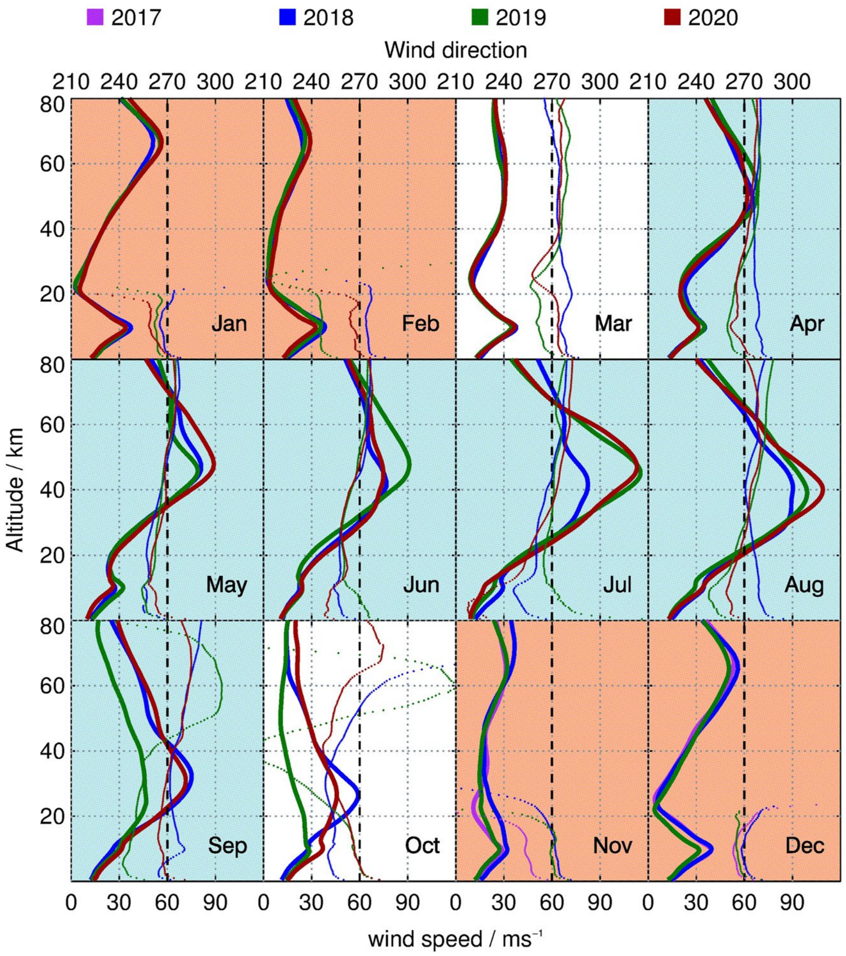

Figure 10. ERA5 monthly mean absolute wind profiles (thick lines) and wind directions above Río Grande (thin lines; the dashed lines mark westerlies). The wind field was truncated at T21 in order to filter out contributions from model-resolved gravity waves (GWs).

When it comes to the horizontal propagation of quasistationary MWs, we have to consider three aspects. First, as discussed above, the horizontal group speed depends on the intrinsic frequency of the wave. As $\hat{\omega}$ approaches f the wave propagates apparently more downwind. "Apparently," because the intrinsic propagation direction is still against the prevailing wind. Second, Sato et al. (2012) have shown that, if there is a component of the wind vector that is perpendicular to the wave vector, a lateral propagation of the wave occurs. Finally, from ray tracing equations it is known that horizontal gradients in the horizontal wind field cause wave vectors to turn. That in combination with the apparent and lateral propagation causes MWs to extend over vast areas downstream of the mountains. Sato et al. (2012) revealed the refraction of MWs into the PNJ. This was also earlier reported by Dunkerton (1984) and more recently by Ehard et al. (2017) studying lidar observations in the vicinity of the Southern Alps of New Zealand. Given these results, the propagation of MWs in the Southern Andes region is a complex subject that will be investigated in more detail in a future study applying raytracing analysis.

5.2. Conservative Growth With Altitude

If there is no wave dissipation, in the presence of a vertically varying background atmosphere the quantity that can be considered constant is the wave pseudomomentum flux (Fritts & Alexander, 2003). The vertical flux of horizontal pseudomomentum is given as

$$F_{\mathrm{Ph}} = \bar{\rho} c_{gz} \frac{E_{\mathrm{p}}}{\hat{\omega}} k_h \tag{20}$$

where $\bar{\rho}$ is the density of the atmosphere. The vertical group velocity for low-frequency GWs is defined as

$$c_{gz} = -\frac{N^2 {k_\mathrm{h}}^2}{m^3 \hat{\omega}}. \tag{21}$$

Substitution of the vertical group speed from Equation 21 in Equation 20 yields

$$F_\mathrm{Ph} = -\bar{\rho} E_\mathrm{p} \frac{k_\mathrm{h}^3}{m^3} \frac{N^2}{\hat{\omega}^2}. \tag{22}$$

It follows that $E_\mathrm{p} \sim \frac{1}{\bar{\rho}} \frac{m}{k_\mathrm{h}} \left(1 + \frac{f^2}{N^2} \frac{m^2}{k_\mathrm{h}^2}\right)$ meaning that as $\bar{\rho}$ decreases with height E_p increases in order to keep the pseudomomentum flux constant. In addition, as we have no information about k_h and we are not able to retrieve a reliable m for each measurement we have to make the assumption that m/k_h remains constant in the entire observational volume. Generally, this is not the case as varying atmospheric background conditions lead to changes in m and k_h (Marks & Eckermann, 1995). To account at least for the thermal structure of the middle atmosphere we calculated conservative growth curves as function of temperature. They represent a rough estimation on the expected growth of wave amplitudes in the absence of dissipation. However, it is obvious that E_p cannot become indefinitely large. At some point there will be wave dissipation for instance when there arises self-induced shear instability or an unstable lapse rate (Dunkerton, 1982). Most of our data show growth rates, which are smaller than conservative growth rates, suggesting possible wave dissipation. Another explanation for smaller growth rates is oblique wave propagation (Kalisch et al., 2014). Here, GWs exit the observational volume at some altitude, causing lower measured E_p values above. Based on our measurement data, we cannot distinguish between the two processes. If waves exit the observational volume at some altitude due to oblique propagation, there is also a certain possibility that waves can enter the volume. This convergence can lead to locally increased E_p values and may even result in growth rates larger than conservative growth rates. This might be the case in the extreme energy profile in the lower stratosphere in September as shown in Figure 7.

5.3. Distribution of Vertical Wavelengths

Most lidar studies dealing with GWs have focused on temperature perturbations with vertical scales of 15–20 km or less. In contrast to that, many satellite studies show GWs with even larger vertical wavelengths (e.g., Preusse et al., 2002). We investigated λ_z of GWs based on sub-seasonal temperature perturbations. which were only detrended by subtraction of annual and semiannual oscillations. Therefore, WAVELET-SCAN results show a broad distribution of vertical wavelengths with values between 5 and 30 km. The presence of waves with vertical wavelengths in the range 20–30 km confirms previous satellite observations. In fact, the majority of detected GWs (58% of the waves) exhibits vertical wavelengths larger than 15 km (Figure 8).

Winter time wind profiles in Figure 10 suggest that according to $m = N/u$ maximum vertical wavelengths of hydrostatic MWs quickly increase toward the wind maximum and shrink above. However, we do not observe this behavior in the KDE as the spatial resolution of the CWT is too poor in order to follow the rapid changes of m. Another consequence of variable vertical wavelengths is the shifting of waves in and out of the spectral window of the Butterworth filter, resulting in variable potential energies despite constant amplitudes. An example is the extreme energy profile in May in Figure 7. On this date, we found vertical wavelengths in the order of 20 km (not shown) in the mid-stratosphere, resulting in a substantial dip in retrieved potential energy at 40 km. If a dominant wave with $\lambda_z > \lambda_\mathrm{cut}$ occurs, its potential energy is underestimated. This affects the E_p distribution such that $\langle E_\mathrm{p} \rangle^{\odot}$ is underestimated and might even result in an underestimation of $\sigma^{\odot}$, $\gamma^{\odot}$ and I_g as waves of larger scales can exhibit larger amplitudes before they become convectively unstable. The transition from $\lambda_z < \lambda_\mathrm{cut}$ to $\lambda_z > \lambda_\mathrm{cut}$ and vice versa occurs most often at the location of the local horizontal wind maximum, that is, at 40–50 km. In addition, the latitudinal position of the PNJ over the Southern Andes can change significantly over the course of several weeks. As the PNJ is responsible for the refraction of waves toward larger vertical wavelengths, this mechanism in combination with a fixed λ_cut might also affect the derivation of potential energies. A study that sheds light on the variability of the E_p distribution and thus also on statistical parameters such as GW intermittency as a function of cutoff-wavelength is in preparation.

5.4. Gravity Wave Activity in the Stratosphere

The filtering of MWs in the summer lower stratosphere is for the most part responsible for a seasonal modulation of GW potential energy in the stratosphere (Figure 6). The presence of a valve layer between March and May is likely the reason why energies only moderately increase in this transition period. When the polar vortex starts to break down, the wind reversal migrates from 80 km in October down to ∼30 km in November. The downward migration of the breaking level causes an earlier decrease of energies at higher altitudes (Kaifler, Lübken, et al., 2015). This is well perceived by the end of winter 2018 in Figure 3b. An exception occurred in September and October of 2019 when a SSW occurred and forced the circulation to reverse about one month earlier than usual (e.g., Dörnbrack et al., 2020; Rapp et al., 2021; Yamazaki et al., 2020).

An annual variation of E_p was also observed above Rothera (67°S, 68°W) (Yamashita et al., 2009). Located on the Antarctic Peninsula, Rothera, 1,500 km away from Río Grande, is alongside Río Gallegos (Llamedo et al., 2019) the closest station where stratospheric (30–45 km) wave activity was investigated using lidar observations. In contrast to CORAL's location with respect to the main mountain ridge, the study at Rothera was conducted on the upstream side of the mountains of the Antarctic Peninsula. Qualitatively, the annual cycle of stratospheric E_p above Rothera is the same as above Río Grande with a maximum in winter and the minimum in summer. Although E_p values cannot be compared one-to-one because the spectra of the GWs contributing to the calculated E_p differ and averaging is different, we still argue that the GW activity above Río Grande is considerably larger than above Rothera. This is consistent with the assumption that MWs primarily propagate above and downsteam the mountains. Hence, smaller E_p values are expected upstream.

Wintertime E_p histograms in the lower and upper stratosphere (Figure 6) exhibit tails toward large values, which are indicative for enhanced GW intermittency. The standard deviation and skewness of the E_p log-normal distribution as well as the Gini coefficient find their maximum in the winter stratosphere, suggesting that GW intermittency is largest there. In the summer lower stratosphere $\sigma^{\odot}$, $\gamma^{\odot}$, and I_g are smaller than in the winter lower stratosphere but still larger than in the summer upper stratosphere. This is most likely due to considerable wave events in November when the MW breaking level is still at about 30 km. Enhanced GW intermittency in the winter stratosphere points to the occurrence of few high-energy events that contribute a large portion to the total potential energy, which is in line with Kaifler et al. (2020).

We compare our E_p profiles with those from previous studies in Figures 11a. In the case of the study by Chu et al. (2018) we computed a mean profile over the months May to September. In addition, we applied a Hann filter with a width of 10 km to E_p profiles. Please note that the profile from Wright et al. (2016) is based on SABER measurements in the spatial domain 49°–59°S and 58°–78°W, while the other profiles are based on lidar data.

We obtained about the same $\langle E_\mathrm{p}\rangle^{\odot}$ profile as in the study by Wright et al. (2016). While Wright et al. (2016) detect waves with $4\,\mathrm{km} < \lambda_z < 30\,\mathrm{km}$ (see Figure 11b) they are only sensitive to waves with $\lambda_\mathrm{h} > 500\,\mathrm{km}$. We, on the other hand, detect waves with $2\,\mathrm{km} < \lambda_z < 15\,\mathrm{km}$ regardless of their horizontal wavelength. The difference in spectral coverage may result in almost congruent profiles. About two times larger energies are found in the stratosphere and lower mesosphere above Río Grande in comparison to Davis station (S. P. Alexander et al., 2011; B. Kaifler, Lübken, et al., 2015). The spectral coverage in the studies by S. P. Alexander et al. (2011) and B. Kaifler, Lübken, et al. (2015) is shifted toward larger vertical wavelengths in comparison to our data, which could explain the factor of 2 difference. There is a factor of 5 difference between energies from Chu et al. (2018) and our study that is probably due to the fact that Chu et al. (2018) only consider GWs with ground-based periods between 3 and 9 h. The study by Mzé et al. (2014) includes GWs at the high frequency end of the spectrum with vertical wavelengths between 1 and 10 km and ground-based periods down to 1 h. The deviations are largest in the stratosphere where energies are about 5 times larger at Río Grande than at Haute Provence, but at 80 km, the profiles are almost identical. This decreasing difference in potential energy might be explained by different GW source spectra at the two locations. In addition to varying spectral coverages, we argue that the large energies in our study compared to other works are the result of larger wave amplitudes at Río Grande due to stronger MW forcing and favorable propagation conditions.

As evident from Figure 1, the stratosphere over Río Grande is an extremely perturbed place. The wind and temperature structure of the atmosphere here create ideal growth conditions for MWs. In the climatological mean, we find the largest potential energies ever reported. Individual cases (see e.g., extreme energy profile

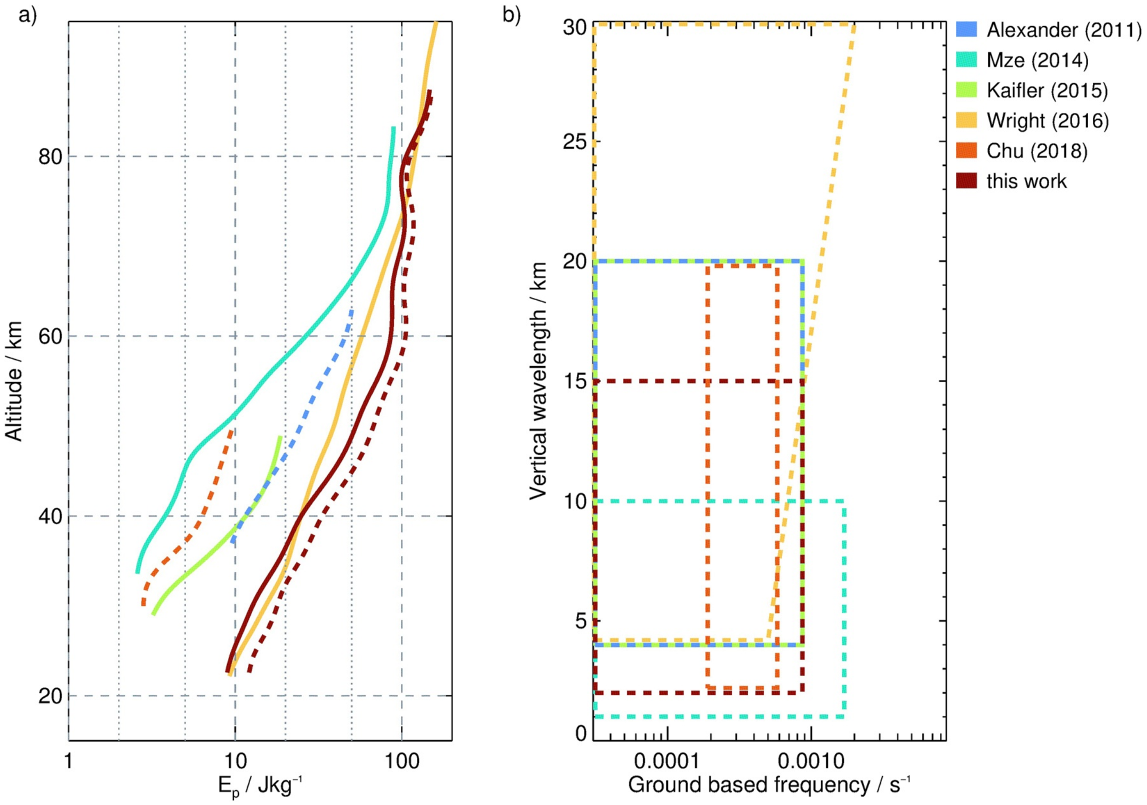

Figure 11. (a) Winter median/geometric mean (solid) and arithmetic mean (dashed) E_p profiles from different publications. (b) Spectral ranges.

in April in Figure 7) show potential energies exceeding 100Jkg^{-1} already at 30 km, which we consider to be the saturation limit in the mesosphere (See Section 5.5). These extraordinary cases lead the E_p distribution and hence are responsible for enhanced GW intermittency ($I_g = 0.44$). We suspect that it is the coincidence of strong forcing of MWs and the relatively stable connection of the PNJ to the tropospheric jet that likely leads to the observed extreme wave amplitudes and makes this region the world's largest stratospheric GW hot spot.

5.5. Gravity Wave Activity in the Mesosphere

An annual variation of wave activity is not only observed in the stratosphere but also in the mesosphere with a semiannual variation superimposed. The summer peak of $\langle E_p \rangle^{\diamond}$ in the upper mesosphere is best explained by non-orographic GWs, as orographic waves are filtered in the lower stratosphere. Their sources may include convection in the troposphere (Alexander & Pfister, 1995; Dewan et al., 1998; Sato, 1993; Taylor & Hapgood, 1988), shear instabilities in the jet exit region (Bühler & McIntyre, 1999; Bühler et al., 1999), and geostrophic adjustment (e.g., Fritts & Luo, 1992). A close alignment of the $\langle E_p \rangle^{\circledcirc}$ profile with conservative growth curves in January and December indicates a conservative propagation of waves in the summer mesosphere. The $\langle E_p \rangle^{\diamond}$ minima in the transition months are probably due to small wind speeds close to zero over a wide range of heights, which can lead to self-induced shear instabilities by GWs (Wilson et al., 1991). A semiannual occurrence of wave activity is also reported by Krebsbach and Preusse (2007) based on SABER measurements. Most recently Sedlak et al. (2020) found that the semiannual variation of wave activity at ~85 km is primarily due to short period GWs (1.0–3.5 h), whereas the annual variation is due to long period GWs (3.5–8.0 h). The 2D wavelet analysis reveals that the winter peak of $\langle E_p \rangle^{\diamond}$ is mainly due to MWs but also an increasing number of apparently up- and downward propagating waves contributes to enhanced potential energies (Table 3).

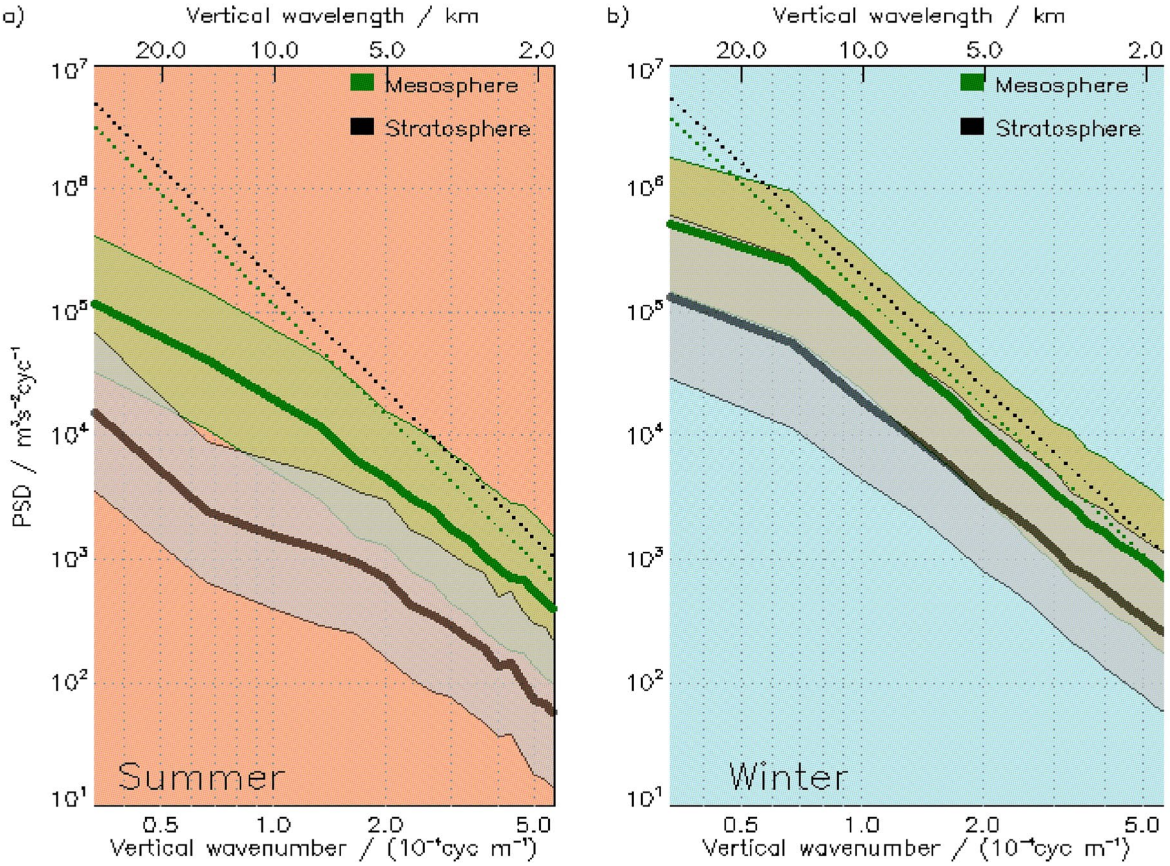

Figure 12. Average power spectral density in the stratosphere (black) and the mesosphere (green) for (a) summer and (b) winter. Saturation limits (dotted lines) are computed according to $\frac{N^2}{10m^3}$. Shaded areas in the background indicate standard deviations.

The constant $\langle E_\mathrm{p}\rangle^{\circledcirc}$ profiles above 60 km suggest that wave amplitudes cannot grow any further and the GW spectrum is saturated. To prove that we determine the power spectral density (PSD) in the stratosphere (20–50 km) and mesosphere (50–80 km) for summer and winter separately (Figure 12). The PSD is calculated as $F(m) = \frac{\Delta z^2}{Z}|\hat{x}(m)|^2$, where $\Delta z = 0.1\,\mathrm{km}$, $Z = 30\,\mathrm{km}$ and $\hat{x}(m)$ is the FFT of the relative sub-seasonal temperature perturbations $\frac{T'}{\bar{T}}$ scaled with $g/N(z)^2$ (Smith et al., 1987; Wilson et al., 1991; S. P. Alexander et al., 2011). In addition, we calculate the saturation limit $\frac{N^2}{10m^3}$ following S. P. Alexander et al. (2011). For that we average monthly mean temperature profiles from Figure 2 over summer and winter, respectively, and compute N according to Equation 5. After that N is averaged over stratospheric and mesospheric altitudes, respectively.

In the summer stratosphere, there is an order of magnitude difference between the average PSD and the saturation limit for short vertical scales around 2 km. The difference increases gradually to two orders of magnitude at vertical scales of 20 km. In winter, the behavior is qualitatively the same but the differences are smaller by a factor of two, which is due to stronger stratospheric wave activity. Wilson et al. (1991) observed the same difference in PSD in the summer stratosphere (30–45 km) but found a similarly low PSD in winter above Haute Provence. At Río Grande in the summer mesosphere, the mean PSD is rather close to the saturation limit for small scales. The saturation limit is actually within the 1σ range at scales ranging from 1.8 to 5 km, but for large scales a difference of one order of magnitude remains. In winter, the mean PSD is very close to the saturation limit and is within the 1σ range at all scales between 1.8 and 20 km. Wilson et al. (1991) observed saturation for scales up to 8 km in the altitude range 60–75 km in winter. S. P. Alexander et al. (2011) showed that only small scales (4 km) reach the saturation limit in the winter mesosphere (49–59 km) above Davis Station. In contrast, Figure 12 reveals that the GW spectrum at Río Grande is saturated for all vertical wavelengths of up to 20 km. This is an outstanding result, as to our knowledge no other study has yet shown saturation up to these large scales. We conclude that the strongly saturated GW spectrum is a combination of both strong forcing and favorable vertical propagation at the GW hot spot in the Southern Andes region.

E_p standard deviations, skewnesses, and Gini coefficients for the winter mesosphere indicate a decreasing GW intermittency from 50 to 80 km (Table 2). In contrast, increasing $\sigma^{\odot}$ and I_g suggest an increasing GW intermittency in summer from 50 to 80 km. Hence, we conclude that saturation of the GW spectrum influences the GW intermittency in the mesosphere. In a saturated spectrum, GW amplitudes cannot grow anymore with altitude, as larger amplitudes cause self-induced instabilities and thus can exist for short periods of time only. If, in the stratosphere, GW amplitudes are modulated in time due to the intermittency of GWs, this means that for large-amplitude waves, saturation of the GW spectrum occurs already at lower altitudes than would be the case for low-amplitude waves. However, the amplitudes in the altitude region where the spectrum is saturated remain approximately at the same level. Hence, we expect that the temporal variability of E_p in the saturation zone is strongly reduced as compared to the variability at lower altitudes. This behavior is clearly visible in our data, which suggests a saturation limit at ∼100 J kg^{-1}. The E_p profile by Mzé et al. (2014) indicates a saturation limit at ∼90 J kg^{-1} above 75 km (Figure 11a), but a saturation zone starting at 60 km was to our knowledge not yet observed. The SABER winter median E_p profile from Wright et al. (2016) shows further increasing values toward 100 km altitude, but differences between the SABER profile and our lidar data are probably due to different observational filters (Alexander, 1998).

The winter mesosphere over Río Grande is characterized by GW dissipation. This becomes evident, for instance, from the extreme wave profiles in Figure 2, which show unstable temperature gradients. But also constant GW potential energies above 60 km and the PSDs shown in Figure 12 indicate a saturated GW spectrum up to scales of 20 km, resulting in the deposition of wave momentum and energy at these altitudes. A fraction of this momentum is likely used to generate secondary GWs. This conclusion is supported by the increasing portion of apparently up- and downward propagating waves.

6. Summary and Conclusions

In this study, we seek to investigate multiple aspects of the Southern Andes GW hot spot. Now, we want to answer our introductory questions and summarize what we can learn from three years of lidar temperature measurements at Río Grande beyond what is already known from previous observations.

6.1. Fraction of MWs

Steady phase lines lasting 3–15 h dominate (53.4%) the observed temperature perturbations at all altitudes, indicating that orographic forcing is the predominant source for the GWs detected by CORAL in the lee of the Andes. As higher mountain peaks are distant, we speculate that the observed MWs belong to the hydrostatic rotating wave regime as defined by Queney (1948) and Gill (1982). If this were indeed the case, air flow across the entire southern Andean ridge can be considered as the waves' source of excitation. Similar observations of the leeward and downstream propagation of horizontally long MWs have been made in the northern hemisphere (Dörnbrack et al., 1999; Kivi et al., 2020), and published comparisons with the ECMWF (Gupta et al., 2021; Gupta et al., 2021; Kaifler et al., 2020; Rapp et al., 2021) support these observational findings.

In addition to steady phase lines, the increasing contribution of apparently up- and downward propagating waves with altitude might be an indication for secondary GWs at mesospheric altitudes (Vadas et al., 2018) or convectively generated GWs from tropical regions (Yuan et al., 2016; Yue et al., 2014) to name possible interpretations.

6.2. Seasonal Variability of GW Potential Energy

The GW potential energies over Río Grande show a seasonal variability as seen in other studies (Baumgarten et al., 2017; Chu et al., 2018; Kaifler, Lübken, et al., 2015; Llamedo et al., 2019; Yamashita et al., 2009). The difference is most pronounced in the lower mesosphere, where we measure 10 times greater energies in winter than in summer. In addition, our measurements also show a semi-annual variation of the GW potential energy in the upper mesosphere as observed by Mzé et al. (2014) and Sedlak et al. (2020).

6.3. Conservative Wave Propagation

GW potential energies in the winter stratosphere are the largest ever reported, which is most likely due to very large initial wave amplitudes and favorable propagation conditions. In the winter stratosphere, GWs propagate conservatively in the climatological mean, that is, their vertical and downstream propagation can be approximately described by linear theory. This is in agreement with previous findings (Alexander et al., 2011; Kaifler, Lübken, et al., 2015; Mzé et al., 2014; Wright et al., 2016). In individual cases, the stratospheric increase of E_p seems to exceed conservative growth rates, which would indicate a lateral propagation of waves through CORAL's field of view.

Above 60 km altitude, major wave dissipation and saturation is indicated by an E_p saturation limit in the order of ~100 J kg^{-1} in winter. A saturated GW spectrum is also evident from the PSD. A limit of the same magnitude was also found in Haute Provence, but it is there only from an altitude of about 75 km (Mzé et al., 2014). In individual cases, constant profiles of GW potential energy close to the saturation limit indicate wave dissipation in the entire observational volume, which is most probably due to breaking of MWs excited by an exceptional strong forcing and excellent propagation conditions.

6.4. GW Intermittency

GW intermittency above Río Grande is largest in the winter stratosphere and reduces with altitude, which is likely related to the saturation of the GW spectrum in the winter mesosphere. This finding is in contrast to the results by Wright et al. (2013) who found almost constant intermittency between 25 and 65 km based on SABER data.

Every winter month, there is at least one temperature profile with exceptional stratospheric temperature deviations from the monthly mean by 25–55 K. Even if these amplitudes are not caused by GWs alone, but presumably by superposition with PWs, to our knowledge they are the largest ever measured. First, these values indicate the exceptional wave energies that can be achieved over the Andes. Second, their presence in the CORAL data set underscores the advantage of high-resolution and high-cadence ground-based lidar measurements.

6.5. Distribution of Vertical Wavelengths

With the assistance of our new diagnostic tool WAVELET-SCAN we have investigated the distribution of vertical wavelengths without focusing only on dominant modes. The majority of waves exhibit vertical wavelengths larger than 15 km, which was used as cutoff wavelength in the E_p analysis. Therefore, we must conclude that the E_p saturation limit, E_p growth rates and parameters like the Gini coefficient are underestimated. A study that will shed light on the variability of the E_p distribution as a function of cutoff-wavelength is in preparation.

As demonstrated in this work, CORAL measurements form an invaluable high-resolution database at the world's strongest GW hot spot. The specific forcing and propagation conditions of the individual GW events in the temperature measurements are still a conundrum, and we hope to solve this puzzle using ray tracing in a future study.

Appendix A: Reconstruction of the Temperature Background

The temperature background is retrieved by means of a harmonic fit with annual and semiannual component. The fit function is given as

$$\overline{T}(t) = T_0 + T_{\mathrm{AO}} \cos(\omega(t - \tau_{\mathrm{AO}})) + T_{SAO} \cos(2\omega(t - \tau_{\mathrm{SAO}})) \tag{A1}$$

with $\omega = 2\pi/365\mathrm{d}$. The fit parameters T_0, T_{AO}, T_{SAO}, τ_{AO}, and τ_{SAO} are determined independently for each height in steps of 100 m. Prior to the application of the least-square harmonic fit, we compute a composite of the temperature data by averaging nightly mean profiles with the same day of year. In addition, only those measurements are taken into account which are longer than 3 h in order to ensure that measurements are representative means. That way the influence of uncorrelated temperature variability, for example, PWs and GWs, is reduced. The result of the harmonic fit with annual and semiannual component is shown in Figure A1.

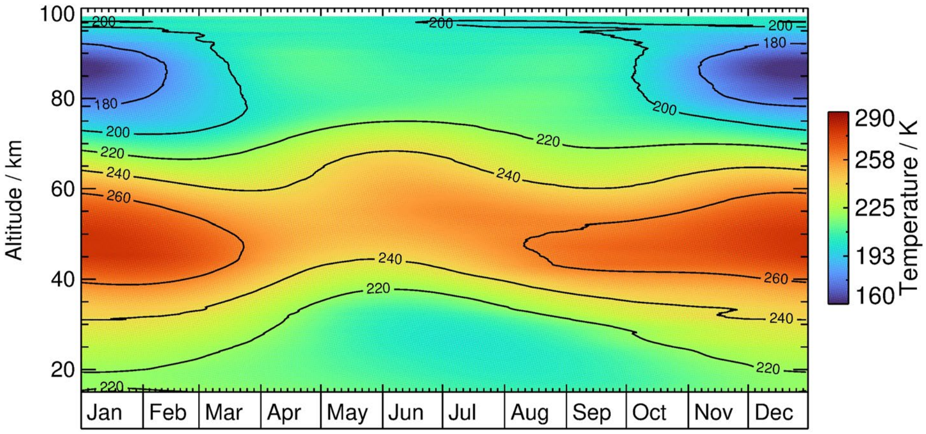

Figure A1. Temperature background determined by means of a harmonic fit with annual and semiannual components.

Appendix B: Testing of WAVELET-SCAN With Artificial Temperature Data

WAVELET-SCAN combines the CWT with DBSCAN in order to retrieve coherent wave packets from lidar temperature data. To validate its performance, we apply WAVELET-SCAN to a test case with artificial temperature data. The artificial wavefield is composed of a stationary MW with a variable vertical wavelength and amplitude as well as one superimposed propagating wave.

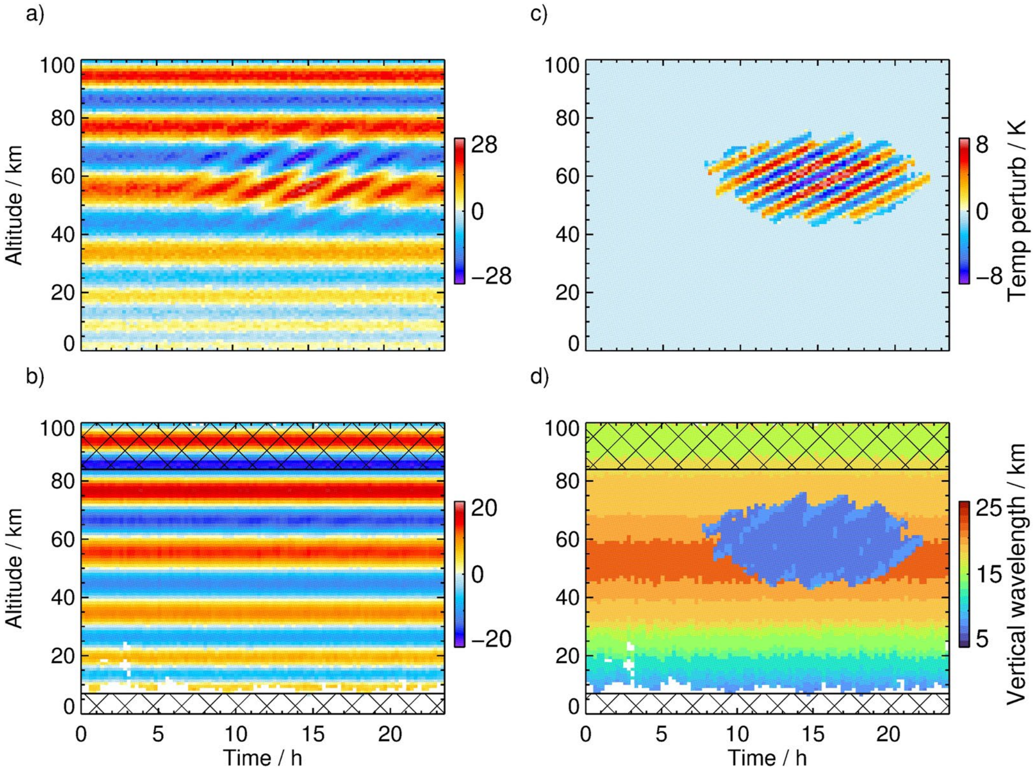

Figure B1. Artificial temperature perturbations (a), reconstructed stationary wave (b), reconstructed propagating wave (c), and retrieved vertical wavelengths (d). Hatched areas mark the cone of influence (COI).

$$
\begin{aligned}
T_{\mathrm{art}}(t,\ z) = {} & \frac{A_{\mathrm{sw}}}{1 - \exp\left(-\dfrac{z - z_{\mathrm{sw}}}{2H_s}\right)} \sin\left(\int_0^z m_{\mathrm{sw}}(\tilde{z}) d\tilde{z}\right) \\
& + A_{\mathrm{pw}} \exp\left(-\frac{z - z_{\mathrm{pw}}}{2\sigma_z^2} - \frac{t - t_{\mathrm{pw}}}{2\sigma_t^2}\right) \cos(m_{\mathrm{pw}} z - \omega_{\mathrm{pw}} t) \\
& + \Delta T_{\mathrm{art}}
\end{aligned}
\tag{B1}
$$

with $A_{\mathrm{sw}} = 20$ K, $z_{\mathrm{sw}} = 30$ km, $H_s = 7.4$ km, $m_{\mathrm{sw}}(z) = 2\pi/\lambda_{\mathrm{sw}}(z)$, $A_{\mathrm{pw}} = 8$ K, $z_{\mathrm{pw}} = 60$ km, $t_{\mathrm{pw}} = 15$ h, $m_{\mathrm{pw}} = 2\pi/8\mathrm{km}$, $\omega_{\mathrm{pw}} = 2\pi/3\mathrm{h}$, $\sigma_z = 10$ km, $\sigma_t = 5$ h, ΔT_{art} is random noise with a standard deviation of 1 K. The vertical wavelength of the stationary wave varies according to

$$
\lambda_{\mathrm{sw}}(z) = \begin{cases} 5\mathrm{km} + 0.4z & \text{for } z \le 50\mathrm{km} \\ 35\mathrm{km} - 0.2z & \text{for } z > 50\mathrm{km}. \end{cases}
\tag{B2}
$$

Figure B1 shows the artificial temperature perturbations, retrieved vertical wavelengths as well as the two wave packets separated by WAVELET-SCAN.

This validation demonstrates that WAVELET-SCAN is capable of separating superimposed wave packets very accurately. Although the modeled linear increase and decrease of λ_z seems correct, the exact values differ from the input. With $\omega_0 = 4$ the CWT has a good spectral resolution but on the cost of spatial resolution. Hence, if vertical wavelengths change rapidly with height, retrieved wavelengths must be seen as an average over a certain altitude range.

Appendix C: Uncertainty Calculations

To find out how the temperature error due to photon noise is distributed between the temperature perturbations and the temperature background, we performed a Monte Carlo simulation. It became apparent that about 1/9 of the temperature uncertainty introduced is reflected in the background and 8/9 in the disturbances. Therefore, we define,

$$
\Delta T' = \sqrt{\frac{8}{9}} \Delta T \quad \text{and}
\tag{C1}
$$

$$
\Delta T_{\mathrm{BG}} = \sqrt{\frac{1}{9}} \Delta T + \Delta \bar{T}
\tag{C2}
$$

where the additional term $\Delta \bar{T}$ accounts for the uncertainty due to the subtraction of seasonal oscillations. The uncertainty of the squared relative temperature perturbations is then given as

$$
\Delta T_{\mathrm{r}}' = \frac{2}{T_{\mathrm{BG}}} \left(\frac{|T'|}{T_{\mathrm{BG}}} \Delta T' + \frac{T'^2}{T_{\mathrm{BG}}^2} \Delta T_{\mathrm{BG}} \right).
\tag{C3}
$$

The uncertainty of the squared Brunt Väisälä frequency is given as

$$
\Delta N^2 = \frac{\Delta T_{\mathrm{BG}}}{T_{\mathrm{BG}}} \left(N^2 + \frac{\sqrt{2} g}{\delta z} \right).
\tag{C4}
$$

Finally, the uncertainty of GW potential energy is defined as

$$
\Delta E_{\mathrm{p}} = E_{\mathrm{p}} \frac{\Delta N^2}{N^2} + \frac{1}{2} \frac{g^2}{N^2} \overline{\Delta T_{\mathrm{r}}'},
\tag{C5}
$$

where the overbar denotes that $\Delta T_{\mathrm{r}}'$ is averaged as in Equation 6 and divided by $\sqrt{n_t n_z}$.

Conflict of Interest

The authors declare no conflicts of interest relevant to this study.

Data Availability Statement

Data sets for the reproduction of figures are available as NetCDF files in HALO-DB at https://halo-db.pa.op.dlr.de/mission/111. ECMWF's HRES IFS operational analyses can be freely accessed from https://www.ecmwf.int/en/forecasts/datasets/set-i.

Acknowledgments

R. Reichert thanks the German Research Foundation (DFG) for support through the research unit Multiscale Dynamics of Gravity Waves (MS-GWaves) grant RA 1400/6-1. Initial CORAL observations at Río Grande were supported by ARISE2 (http://ARISE-project.eu), which received funding from the European Commission's H2020 program (grant agreement 653980). This research was partially funded by the DFG via the project MS-GWaves (GW-TP/DO 1020/9-1, PACOG/RA 1400/6-1) and by the German research initiative “Role of the middle atmosphere in climate” (ROMIC) under grant 01LG1206A provided by the Federal Ministry for Education and Research. Access to ECMWF data was granted through the special project “Deep Vertical Propagation of Internal Gravity Waves.” Open access funding enabled and organized by Projekt DEAL.

References

Alexander, M. J. (1998). Interpretations of observed climatological patterns in stratospheric gravity wave variance. *Journal of Geophysical Research*, *103*(D8), 8627–8640. https://doi.org/10.1029/97jd03325

Alexander, M. J., & Barnet, C. (2007). Using satellite observations to constrain parameterizations of gravity wave effects for global models. *Journal of the Atmospheric Sciences*, *64*(5), 1652–1665. https://doi.org/10.1175/JAS3897.1

Alexander, M. J., & Pfister, L. (1995). Gravity wave momentum flux in the lower stratosphere over convection. *Geophysical Research Letters*, *22*(15), 2029–2032. https://doi.org/10.1029/95gl01984

Alexander, S. P., Klekociuk, A. R., & Murphy, D. J. (2011). Rayleigh lidar observations of gravity wave activity in the winter upper stratosphere and lower mesosphere above Davis, Antarctica (69°S, 78°E). *Journal of Geophysical Research*, *116*(D13). https://doi.org/10.1029/2010JD015164

Alexander, S. P., Sato, K., Watanabe, S., Kawatani, Y., & Murphy, D. J. (2016). Southern Hemisphere extratropical gravity wave sources and intermittency revealed by a middle-atmosphere general circulation model. *Journal of the Atmospheric Sciences*, *73*(3), 1335–1349. https://doi.org/10.1175/jas-d-15-0149.1

Alexander, S. P., Tsuda, T., & Kawatani, Y. (2008). COSMIC GPS observations of Northern Hemisphere winter stratospheric gravity waves and comparisons with an atmospheric general circulation model. *Geophysical Research Letters*, *35*(10). https://doi.org/10.1029/2008gl033174

Baumgaertner, A. J. G., & McDonald, A. J. (2007). A gravity wave climatology for Antarctica compiled from Challenging Minisatellite Payload/Global Positioning System (CHAMP/GPS) radio occultations. *Journal of Geophysical Research*, *112*(D5). https://doi.org/10.1029/2006JD007504

Baumgarten, K., Gerding, M., & Lübken, F.-J. (2017). Seasonal variation of gravity wave parameters using different filter methods with daylight lidar measurements at midlatitudes. *Journal of Geophysical Research: Atmospheres*, *122*(5), 2683–2695. https://doi.org/10.1002/2016jd025916

Bramberger, M., Dörnbrack, A., Bossert, K., Ehard, B., Fritts, D. C., Kaifler, B., et al. (2017). Does strong tropospheric forcing cause large-amplitude mesospheric gravity waves? A DEEPWAVE case study. *Journal of Geophysical Research: Atmospheres*, *122*(21), 11–422. https://doi.org/10.1002/2017jd027371

Bühler, O. (2014). *Waves and mean flows*. Cambridge University Press.

Bühler, O., & McIntyre, M. E. (1999). On shear-generated gravity waves that reach the mesosphere. Part II: Wave propagation. *Journal of the Atmospheric Sciences*, *56*(21), 3764–3773. https://doi.org/10.1175/1520-0469(1999)056<3764:osggwt>2.0.co;2

Bühler, O., McIntyre, M. E., & Scinocca, J. F. (1999). On shear-generated gravity waves that reach the mesosphere. Part I: Wave generation. *Journal of the Atmospheric Sciences*, *56*(21), 3749–3763. https://doi.org/10.1175/1520-0469(1999)056<3749:osggwt>2.0.co;2

Chen, C., & Chu, X. (2017). Two-dimensional Morlet wavelet transform and its application to wave recognition methodology of automatically extracting two-dimensional wave packets from lidar observations in Antarctica. *Journal of Atmospheric and Solar-Terrestrial Physics*, *162*, 28–47. https://doi.org/10.1016/j.jastp.2016.10.016

Chu, X., Zhao, J., Lu, X., Harvey, V. L., Jones, R. M., Becker, E. W., et al. (2018). Lidar observations of stratospheric gravity waves from 2011 to 2015 at McMurdo (77.84°S, 166.69°E), Antarctica: 2. potential energy densities, lognormal distributions, and seasonal variations. *Journal of Geophysical Research: Atmospheres*, *123*(15), 7910–7934. https://doi.org/10.1029/2017jd027386

Dewan, E. M., Picard, R. H., O'Neil, R. R., Gardiner, H. A., Gibson, J., Mill, J. D., & Gallery, W. O. (1998). MSX satellite observations of thunderstorm-generated gravity waves in mid-wave infrared images of the upper stratosphere. *Geophysical Research Letters*, *25*(7), 939–942. https://doi.org/10.1029/98gl00640

Dörnbrack, A., Gisinger, S., & Kaifler, B. (2017). On the interpretation of gravity wave measurements by ground-based lidars. *Atmosphere*, *8*(3), 49. https://doi.org/10.3390/atmos8030049

Dörnbrack, A., Kaifler, B., Kaifler, N., Rapp, M., Wildmann, N., Garhammer, M., & Austin, E. J. (2020). Unusual appearance of mother-of-pearl clouds above El Calafate, Argentina (50° 21′S, 72°16′W). *Weather*, *75*(12), 378–388. https://doi.org/10.1002/wea.3863

Dörnbrack, A., Leutbecher, M., Kivi, R., & Kyrö, E. (1999). Mountain-wave-induced record low stratospheric temperatures above northern Scandinavia. *Tellus A: Dynamic Meteorology and Oceanography*, *51*(5), 951–963. https://doi.org/10.1034/j.1600-0870.1999.00028.x

Dunkerton, T. J. (1982). Wave transience in a compressible atmosphere. Part III: The saturation of internal gravity waves in the mesosphere. *Journal of the Atmospheric Sciences*, *39*(5), 1042–1051.

Dunkerton, T. J. (1984). Inertia–gravity waves in the stratosphere. *Journal of the Atmospheric Sciences*, *41*(23), 3396–3404. https://doi.org/10.1175/1520-0469(1984)041<3396:iwits>2.0.co;2

Eckermann, S. D., & Preusse, P. (1999). Global measurements of stratospheric mountain waves from space. *Science*, *286*(5444), 1534–1537. https://doi.org/10.1126/science.286.5444.1534

Ehard, B., Kaifler, B., Dörnbrack, A., Preusse, P., Eckermann, S. D., Bramberger, M., et al. (2017). Horizontal propagation of large-amplitude mountain waves into the polar night jet. *Journal of Geophysical Research: Atmospheres*, *122*(3), 1423–1436. https://doi.org/10.1002/2016jd025621

Ehard, B., Kaifler, B., Kaifler, N., & Rapp, M. (2015). Evaluation of methods for gravity wave extraction from middle-atmospheric lidar temperature measurements. *Atmospheric Measurement Techniques*, *8*(11), 4645–4655. https://doi.org/10.5194/amt-8-4645-2015

Ern, M., Preusse, P., Alexander, M. J., & Warner, C. D. (2004). Absolute values of gravity wave momentum flux derived from satellite data. *Journal of Geophysical Research*, *109*(D20).

Ester, M., Kriegel, H.-P., Sander, J., & Xu, X. (1996). A density-based algorithm for discovering clusters in large spatial databases with noise. In *Kdd* (pp. 226–231).

Fritts, D. C., & Alexander, M. J. (2003). Gravity wave dynamics and effects in the middle atmosphere. *Reviews of Geophysics*, *41*(1). https://doi.org/10.1029/2001rg000106

Fritts, D. C., & Luo, Z. (1992). Gravity wave excitation by geostrophic adjustment of the jet stream. Part I: Two-dimensional forcing. *Journal of the Atmospheric Sciences*, *49*(8), 681–697. https://doi.org/10.1175/1520-0469(1992)049<0681:gwebga>2.0.co;2

Gardner, C. S., & Taylor, M. J. (1998). Observational limits for lidar, radar, and airglow imager measurements of gravity wave parameters. *Journal of Geophysical Research*, *103*(D6), 6427–6437. https://doi.org/10.1029/97jd03378

Gerding, M., Höffner, J., Lautenbach, J., Rauthe, M., & Lübken, F.-J. (2008). Seasonal variation of nocturnal temperatures between 1 and 105 km altitude at 50°N observed by lidar. *Atmospheric Chemistry and Physics*, *8*(24), 7465–7482. https://doi.org/10.5194/acp-8-7465-2008

Gill, A. E. (1982). *Atmosphere-ocean dynamics*. Academic Press

Gupta, A., Birner, T., Dörnbrack, A., & Polichtchouk, I. (2021). Importance of gravity wave forcing for springtime southern polar vortex breakdown as revealed by ERA5. *Geophysical Research Letters*, *48*(10), e2021GL092762. https://doi.org/10.1029/2021gl092762

Heale, C. J., Bossert, K., Vadas, S. L., Hoffmann, L., Dörnbrack, A., Stober, G., & Jacobi, C. (2020). Secondary gravity waves generated by breaking mountain waves over Europe. *Journal of Geophysical Research: Atmospheres*, *125*(5), e2019JD031662. https://doi.org/10.1029/2019jd031662

Hertzog, A., Alexander, M. J., & Plougonven, R. (2012). On the intermittency of gravity wave momentum flux in the stratosphere. *Journal of the Atmospheric Sciences*, *69*(11), 3433–3448. https://doi.org/10.1175/jas-d-12-09.1

Hindley, N. P., Wright, C. J., Hoffmann, L., Moffat-Griffin, T., & Mitchell, N. J. (2020). An 18-year climatology of directional stratospheric gravity wave momentum flux from 3-D satellite observations. *Geophysical Research Letters*, *47*, e2020GL089557

Hindley, N. P., Wright, C. J., Smith, N. D., & Mitchell, N. J. (2015). The southern stratospheric gravity wave hot spot: Individual waves and their momentum fluxes measured by COSMIC GPS-RO. *Atmospheric Chemistry and Physics*, *15*(14).

Hoffmann, L., Xue, X., & Alexander, M. J. (2013). A global view of stratospheric gravity wave hotspots located with Atmospheric Infrared Sounder observations. *Journal of Geophysical Research*, *118*(2), 416–434. https://doi.org/10.1029/2012jd018658

Hoffmann, P., Becker, E., Singer, W., & Placke, M. (2010). Seasonal variation of mesospheric waves at northern middle and high latitudes. *Journal of Atmospheric and Solar-Terrestrial Physics*, *72*(14–15), 1068–1079. https://doi.org/10.1016/j.jastp.2010.07.002

Jiang, Q., Doyle, J. D., Reinecke, A., Smith, R. B., & Eckermann, S. D. (2013). A modeling study of stratospheric waves over the Southern Andes and Drake Passage. *Journal of the Atmospheric Sciences*, *70*(6), 1668–1689. https://doi.org/10.1175/jas-d-12-0180.1

Kaifler, B., & Kaifler, N. (2021). A Compact Rayleigh Autonomous Lidar (CORAL) for the middle atmosphere. *Atmospheric Measurement Techniques*, *14*(2), 1715–1732. https://doi.org/10.5194/amt-14-1715-2021

Kaifler, B., Kaifler, N., Ehard, B., Dörnbrack, A., Rapp, M., & Fritts, D. C. (2015). Influences of source conditions on mountain wave penetration into the stratosphere and mesosphere. *Geophysical Research Letters*, *42*(21), 9488–9494. https://doi.org/10.1002/2015gl066465

Kaifler, B., Lübken, F.-J., Höffner, J., Morris, R. J., & Viehl, T. P. (2015). Lidar observations of gravity wave activity in the middle atmosphere over Davis (69°S, 78°E), Antarctica. *Journal of Geophysical Research: Atmospheres*, *120*(10), 4506–4521. https://doi.org/10.1002/2014JD022879

Kaifler, N., Kaifler, B., Dörnbrack, A., Rapp, M., Hormaechea, J. L., & de la Torre, A. (2020). Lidar observations of large-amplitude mountain waves in the stratosphere above Tierra del Fuego, Argentina. *Scientific Reports*, *10*(1), 1–10. https://doi.org/10.1038/s41598-020-71443-7

Kaifler, N., Kaifler, B., Ehard, B., Gisinger, S., Dörnbrack, A., Rapp, M., et al. (2017). Observational indications of downward-propagating gravity waves in middle atmosphere lidar data. *Journal of Atmospheric and Solar-Terrestrial Physics*, *162*, 16–27. https://doi.org/10.1016/j.jastp.2017.03.003

Kaifler, N., Kaifler, B., Wilms, H., Rapp, M., Stober, G., & Jacobi, C. (2018). Mesospheric temperature during the extreme mid-latitude noctilucent cloud event on 18/19 July 2016. *Journal of Geophysical Research: Atmospheres*. https://doi.org/10.1029/2018JD029717

Kalisch, S., Preusse, P., Ern, M., Eckermann, S. D., & Riese, M. (2014). Differences in gravity wave drag between realistic oblique and assumed vertical propagation. *Journal of Geophysical Research: Atmospheres*, *119*(17), 10–081. https://doi.org/10.1002/2014jd021779

Kivi, R., Dörnbrack, A., Sprenger, M., & Vömel, H. (2020). Far-ranging impact of mountain waves excited over greenland on stratospheric dehydration and rehydration. *Journal of Geophysical Research: Atmospheres*, *125*(18), e2020JD033055. https://doi.org/10.1029/2020jd033055

Kogure, M., Yue, J., Nakamura, T., Hoffmann, L., Vadas, S. L., Tomikawa, Y., & Janches, D. (2020). First direct observational evidence for secondary gravity waves generated by mountain waves over the Andes. *Geophysical Research Letters*, *47*(17), e2020GL088845. https://doi.org/10.1029/2020gl088845

Krebsbach, M., & Preusse, P. (2007). Spectral analysis of gravity wave activity in SABER temperature data. *Geophysical Research Letters*, *34*(3). https://doi.org/10.1029/2006gl028040

Kruse, C. G., Smith, R. B., & Eckermann, S. D. (2016). The midlatitude lower-stratospheric mountain wave "valve layer". *Journal of the Atmospheric Sciences*, *73*(12), 5081–5100. https://doi.org/10.1175/jas-d-16-0173.1

Lindzen, R. S. (1981). Turbulence and stress owing to gravity wave and tidal breakdown. *Journal of Geophysical Research: Oceans*, *86*(C10), 9707–9714. https://doi.org/10.1029/jc086ic10p09707

Llamedo, P., Salvador, J., de la Torre, A., Quiroga, J., Alexander, P., Hierro, R., & Quel, E. (2019). 11 years of rayleigh lidar observations of gravity wave activity above the southern tip of South America. *Journal of Geophysical Research: Atmospheres*, *124*(2), 451–467. https://doi.org/10.1029/2018jd028673

Marks, C. J., & Eckermann, S. D. (1995). A three-dimensional nonhydrostatic ray-tracing model for gravity waves: Formulation and preliminary results for the middle atmosphere. *Journal of the Atmospheric Sciences*, *52*(11), 1959–1984. https://doi.org/10.1175/1520-0469(1995)05210.1175/1520-0469(1995)052<1959:atdnrt>2.0.co;2

Minamihara, Y., Sato, K., & Tsutsumi, M. (2020). Intermittency of gravity waves in the Antarctic troposphere and lower stratosphere revealed by the PANSY radar observation. *Journal of Geophysical Research: Atmospheres*, *125*(15), e2020JD032543. https://doi.org/10.1029/2020jd032543

Mixa, T., Dörnbrack, A., & Rapp, M. (2021). Nonlinear simulations of gravity wave tunneling and breaking over Auckland Island. *Journal of the Atmospheric Sciences*, *78*(5), 1567–1582. https://doi.org/10.1175/jas-d-20-0230.1

Mzé, N., Hauchecorne, A., Keckhut, P., & Thétis, M. (2014). Vertical distribution of gravity wave potential energy from long-term Rayleigh lidar data at a northern middle-latitude site. *Journal of Geophysical Research: Atmospheres*, *119*(21), 12069–12083. https://doi.org/10.1002/2014JD022035

Nappo, C. J. (2002). *An introduction to atmospheric gravity waves (No. Bd. 1)*. Academic Press. Retrieved from https://books.google.de/books?id=I6KDVUU3myoC

Ohneiser, K., Ansmann, A., Baars, H., Seifert, P., Barja, B., Jimenez, C., et al. (2020). Smoke of extreme Australian bushfires observed in the stratosphere over Punta Arenas, Chile, in January 2020: Optical thickness, lidar ratios, and depolarization ratios at 355 and 532 nm. *Atmospheric Chemistry and Physics*, *20*(13), 8003–8015. https://doi.org/10.5194/acp-20-8003-2020

Parzen, E. (1962). On Estimation of a Probability Density Function and Mode. *The Annals of Mathematical Statistics*, *33*(3), 1065–1076. https://doi.org/10.1214/aoms/1177704472

Plougonven, R., Hertzog, A., & Guez, L. (2013). Gravity waves over Antarctica and the Southern Ocean: Consistent momentum fluxes in mesoscale simulations and stratospheric balloon observations. *Quarterly Journal of the Royal Meteorological Society*, *139*(670), 101–118. https://doi.org/10.1002/qj.1965

Preusse, P., Dörnbrack, A., Eckermann, S. D., Riese, M., Schaeler, B., Bacmeister, J. T., & Grossmann, K. U. (2002). Space-based measurements of stratospheric mountain waves by CRISTA 1. Sensitivity, analysis method, and a case study. *Journal of Geophysical Research*, *107*(D23). https://doi.org/10.1029/2001jd000699

Queney, P. (1948). The problem of air flow over mountains: A summary of theoretical studies. *Bulletin of the American Meteorological Society*, *29*(1), 16–26. https://doi.org/10.1175/1520-0477-29.1.16

Rapp, M., Dörnbrack, A., & Kaifler, B. (2018). An intercomparison of stratospheric gravity wave potential energy densities from METOP GPS radio occultation measurements and ECMWF model data. *Atmospheric Measurement Techniques*, *11*(2), 1031. https://doi.org/10.5194/amt-11-1031-2018

Rapp, M., Kaifler, B., Dörnbrack, A., Gisinger, S., Mixa, T., Reichert, R., et al. (2021). SOUTHTRAC-GW: An airborne field campaign to explore gravity wave dynamics at the world's strongest hotspot. *Bulletin of the American Meteorological Society*, *102*(4), E871–E893. https://doi.org/10.1175/bams-d-20-0034.1

Rauthe, M., Gerding, M., & Lübken, F.-J. (2008). Seasonal changes in gravity wave activity measured by lidars at mid-latitudes. *Atmospheric Chemistry and Physics*, *8*(22), 6775–6787. https://doi.org/10.5194/acp-8-6775-2008

Reichert, R., Kaifler, B., Kaifler, N., Rapp, M., Pautet, P.-D., Taylor, M. J., & Kivi, R. (2019). Retrieval of intrinsic mesospheric gravity wave parameters using lidar and airglow temperature and meteor radar wind data. *Atmospheric Measurement Techniques*, *12*(11), 5997–6015. https://doi.org/10.5194/amt-12-5997-2019

Rosenblatt, M. (1956). Remarks on some nonparametric estimates of a density function. *The Annals of Mathematical Statistics*, *27*(3), 832–837. https://doi.org/10.1214/aoms/1177728190

Sato, K. (1993). Small-scale wind disturbances observed by the MU radar during the passage of Typhoon Kelly. *Journal of the Atmospheric Sciences*, *50*(4), 518–537. https://doi.org/10.1175/1520-0469(1993)050<0518:sswdob>2.0.co;2

Sato, K., Tateno, S., Watanabe, S., & Kawatani, Y. (2012). Gravity wave characteristics in the Southern Hemisphere revealed by a high-resolution middle-atmosphere general circulation model. *Journal of the Atmospheric Sciences*, *69*(4), 1378–1396. https://doi.org/10.1175/jas-d-11-0101.1

Sato, K., Watanabe, S., Kawatani, Y., Tomikawa, Y., Miyazaki, K., & Takahashi, M. (2009). On the origins of mesospheric gravity waves. *Geophysical Research Letters*, *36*(19).

Schoeberl, M. R. (1985). The penetration of mountain waves into the middle atmosphere. *Journal of the Atmospheric Sciences*, *42*(24), 2856–2864. https://doi.org/10.1175/1520-0469(1985)042<2856:tpomwi>2.0.co;2

Sedlak, R., Zuhr, A., Schmidt, C., Wüst, S., Bittner, M., Didebulidze, G. G., & Price, C. (2020). Intra-annual variations of spectrally resolved gravity wave activity in the upper mesosphere/lower thermosphere (UMLT) region. *Atmospheric Measurement Techniques*, *13*(9), 5117–5128. https://doi.org/10.5194/amt-13-5117-2020

Smith, S. A., Fritts, D. C., & Vanzandt, T. E. (1987). Evidence for a saturated spectrum of atmospheric gravity waves. *Journal of the Atmospheric Sciences*, *44*(10), 1404–1410. https://doi.org/10.1175/1520-0469(1987)044<1404:efasso>2.0.co;2

Strelnikova, I., Almowafy, M., Baumgarten, G., Baumgarten, K., Ern, M., Gerding, M., & Lübken, F.-J. (2021). Seasonal cycle of gravity wave potential energy densities from lidar and satellite observations at 59° and 69°N. *Journal of the Atmospheric Sciences*, *78*(4), 1359–1386. https://doi.org/10.1175/jas-d-20-0247.1

Strogatz, S. H. (1996). *Nonlinear dynamics and chaos* (p. 932).

Taylor, M. J., & Hapgood, M. A. (1988). Identification of a thunderstorm as a source of short period gravity waves in the upper atmospheric nightglow emissions. *Planetary and Space Science*, *36*(10), 975–985. https://doi.org/10.1016/0032-0633(88)90035-9

Torrence, C., & Compo, G. P. (1998). A practical guide to wavelet analysis. *Bulletin of the American Meteorological Society*, *79*(1), 61–78. https://doi.org/10.1175/1520-0477(1998)07910.1175/1520-0477(1998)079<0061:apgtwa>2.0.co;2

Torrésani, B. (1995). *Analyse continue par ondelettes*. Éditions du CNRS. EDP sciences.

Vadas, S. L., & Becker, E. (2019). Numerical modeling of the generation of tertiary gravity waves in the mesosphere and thermosphere during strong mountain wave events over the Southern Andes. *Journal of Geophysical Research: Space Physics*, *124*(9), 7687–7718. https://doi.org/10.1029/2019ja026694

Vadas, S. L., Zhao, J., Chu, X., & Becker, E. (2018). The excitation of secondary gravity waves from local body forces: Theory and observation. Journal of Geophysical Research. *Atmospheres*, *123*(17), 9296–9325. https://doi.org/10.1029/2017jd027970

Whiteway, J. A., & Carswell, A. I. (1995). Lidar observations of gravity wave activity in the upper stratosphere over Toronto. *Journal of Geophysical Research*, *100*(D7), 14113–14124. https://doi.org/10.1029/95jd00511

Whiteway, J. A., Duck, T. J., Donovan, D. P., Bird, J. C., Pal, S. R., & Carswell, A. I. (1997). Measurements of gravity wave activity within and around the Arctic stratospheric vortex. *Geophysical Research Letters*, *24*(11), 1387–1390. https://doi.org/10.1029/97gl01322

Wilson, R., Chanin, M. L., & Hauchecorne, A. (1991). Gravity waves in the middle atmosphere observed by Rayleigh lidar: 2. Climatology. *Journal of Geophysical Research*, *96*(D3), 5169–5183. https://doi.org/10.1029/90JD02610

Wright, C. J., Hindley, N. P., Hoffmann, L., Alexander, M. J., & Mitchell, N. J. (2017). Exploring gravity wave characteristics in 3-D using a novel S-transform technique: AIRS/Aqua measurements over the Southern Andes and Drake Passage. *Atmospheric Chemistry and Physics*, *17*(13), 8553–8575. https://doi.org/10.5194/acp-17-8553-2017

Wright, C. J., Hindley, N. P., Moss, A. C., & Mitchell, N. J. (2016). Multi-instrument gravity-wave measurements over Tierra del Fuego and the Drake Passage—Part 1: Potential energies and vertical wavelengths from AIRS, COSMIC, HIRDLS, MLS-Aura, SAAMER, SABER and radiosondes. *Measurement Techniques*, *9*, 877–908. https://doi.org/10.5194/amt-9-877-2016

Wright, C. J., Osprey, S. M., & Gille, J. C. (2013). Global observations of gravity wave intermittency and its impact on the observed momentum flux morphology. *Journal of Geophysical Research*, *118*(19), 10–980. https://doi.org/10.1002/jgrd.50869

Yamashita, C., Chu, X., Liu, H.-L., Espy, P. J., Nott, G. J., & Huang, W. (2009). Stratospheric gravity wave characteristics and seasonal variations observed by lidar at the South Pole and Rothera, Antarctica. *Journal of Geophysical Research*, *114*(D12).

Yamazaki, Y., Matthias, V., Miyoshi, Y., Stolle, C., Siddiqui, T., Kervalishvili, G., et al. (2020). September 2019 Antarctic sudden stratospheric warming: Quasi-6-day wave burst and ionospheric effects. *Geophysical Research Letters*, *47*(1), e2019GL086577. https://doi.org/10.1029/2019gl086577

Yuan, T., Heale, C. J., Snively, J. B., Cai, X., Pautet, P.-D., Fish, C., et al. (2016). Evidence of dispersion and refraction of a spectrally broad gravity wave packet in the mesopause region observed by the Na lidar and Mesospheric Temperature Mapper above Logan, Utah. *Journal of Geophysical Research: Atmospheres*, *121*(2), 579–594. https://doi.org/10.1002/2015jd023685

Yuan, T., Solomon, S. C., She, C.-Y., Krüeger, D. A., & Liu, H.-L. (2019). The long-term trends of nocturnal mesopause temperature and altitude revealed by Na lidar observations between 1990 and 2018 at midlatitude. *Journal of Geophysical Research: Atmospheres*, *124*(12), 5970–5980. https://doi.org/10.1029/2018jd029828

Yue, J., Miller, S. D., Hoffmann, L., & Straka, W. C., III (2014). Stratospheric and mesospheric concentric gravity waves over tropical cyclone Mahasen: Joint AIRS and VIIRS satellite observations. *Journal of Atmospheric and Solar-Terrestrial Physics*, *119*, 83–90. https://doi.org/10.1016/j.jastp.2014.07.003.C

Zhao, J., Chu, X., Chen, C., Lu, X., Fong, W., Yu, Z., & Dörnbrack, A. (2017). Lidar observations of stratospheric gravity waves from 2011 to 2015 at McMurdo (77.84° S, 166.69° E), Antarctica: 1. Vertical wavelengths, periods, and frequency and vertical wave number spectra. *Journal of Geophysical Research: Atmospheres*, *122*(10), 5041–5062. https://doi.org/10.1002/2016jd026368